

Contrasting sulfidization in the turbidite and hemipelagic sediments of Bengal Fan

S.Volvoikar¹, A. Mazumdar^{1*}, A. Peketi¹, P. Dewangan¹, B. Sawant¹, A. Manaskanya¹, H. Goswami², D. Das³, S. Pujari¹

¹Geological Oceanography, CSIR-National Institute of Oceanography, Dona Paula,
Goa-403004, India

²School of Physical, Chemical & Applied Sciences, Department of Earth Sciences
Pondicherry University, Puducherry-605014, India

³Presidency University, 86/1, College Street, Kolkata 700 073, India

*Correspondence: maninda@nio.org

Abstract

We report for the first time, contrasting sulfidization profiles in a sedimentary sequence comprising of clay-silt turbidites and hemipelagic dominated deposits in a channel-levee complex of the middle Bengal Fan. The results show the focusing of acid volatile sulfur (AVS), elemental sulfur contents and marked increase in total reducible sulfur concentrations within the clay-silt turbidite rich zone relative to the overlying hemipelagic rich zone. The large spread in $\delta^{34}\text{S}_{\text{AVS}}$ (-36.6 to +64.4‰) and $\delta^{34}\text{S}_{\text{CRS}}$ (-43.7 to +39 ‰) coupled with ^{34}S enrichment spikes in turbidites dominated zone are tell-tale signatures of rapid consumption of pore-water SO_4^{2-} reduction in a closed system conditions created by turbidite depositions. In contrast, $\delta^{34}\text{S}_{\text{CRS}}$ values ranging from -50 to +2.8 ‰ recorded in the hemipelagic rich zone suggest dominantly early-diagenetic pyritization close to the sediment-water interface. The present study signifies the importance of turbidite fan sedimentation in the biogeochemical cycle of sulfur, carbon, and iron and enhances the scope of global Fe-S-C burial estimation in the marinereal.

Keywords: sulfur isotope, turbidite, hemipelagic, Bengal fan, iron, sulfate reduction

1. Introduction

Bengal fan is the largest submarine fan with length and width of 3000 and 1430 km, respectively. The Ganga and Brahmaputra rivers along with their tributaries draining the Himalayas and central Tibet (drainage area ~1.7 million km²) are the main sources of terrigenous sediment (1×10^9 ton/y) and organic particulates (Fournier et al., 2017; Galy et al., 2007,2008; Singh, 2017). The fan sedimentation is driven by the turbidity currents across the shelf and through the Swatch-of-No-Ground(SoNG) into the currently active channel-levee system spreading over >2500 km length (Curray and Moore, 1974; Hubscher et al., 1997; Weber et al., 1997). The Bengal Fan typically represents turbidity driven channel-levee complex (Figure 1) characterized by silt and clay-rich turbidites with sand layers close to the active channel axis (Fournier et al. 2017; Schwenk et al., 2005) and hemipelagic sediments enriched in calcareous nannofossils and benthic/planktic foraminifera (France-Lanord et al., 2016; Weber et al., 2003; Weber and Reilly, 2018). The SoNG is the largest submarine canyon, deeply incised into the Bangladesh shelf and connects the active channel-levee system network in the Bengal Fan and its distal area (Subrahmanyam et al., 2008). It acted as a conduit for the sediment dispersal to give rise to the largest fan in the world. The Bengal fan has been widely studied to understand the evolution of the sedimentary packages (16.5 km thick); fan growth in relation to the Himalayan-tectonics; channel activity including channel filling/avulsion; and the influence of climate change on the nature and flux of organic matter (Einsele et al., 1996; Fournier et al. 2017; France-Lanord et al., 1993, 2016; Galy et al. 2007; Krishna et al., 2016; Weber et al., 1997).

The turbidity driven rapid sedimentation of clay-siltcoupled with organic matter burial, typical of the Bengal fan complex (Fournier et al., 2017; Galy et al 2008), is expected to support anaerobic biogeochemical processes in the sediments by accentuating the efficient burial of organic matter (Anschutz et al., 2002; Arndt et al., 2013; Galy et al., 2007; Hartnett et al., 1998) and bioavailable organic molecules like acetate and lactate (products of anaerobic fermentation: Jørgensen & Kasten, 2006). This would trigger the rapid sulfate reduction via microbially driven organoclastic and/or anaerobic methane oxidation (AOM) processes leading to pore-water H₂S build-up ensuing enhanced synthesis of organic bound sulfur compounds (Raven et al., 2016; Warne et al., 2008) and metal sulfides in the sediments primarily represented by Fe-monosulfide and pyrite (Canfield, 1994; Canfield, 2001; Canfield et al., 2005; Claypool, 2004; Jørgensen & Kasten, 2006; Jørgensen et al., 2019). The occurrence of sub-surface methane in the Bengal fan sediments is evident from both geophysical (Fournier et al., 2017; Fauquembergue et al., 2019) and geochemical (Clemens et al., 2016; Peketi et al., 2020) studies.

Although, the Bengal Fan sediments suit to be a major sink for sulfur coupled with iron and carbon, surprisingly, the diagenetic evolution of the Bengal Fan sediments, especially the carbon-sulfur-iron biogeochemical cycle has not received wide attention despite very high terrestrial organic flux. Here, we report for the first time a comprehensive analysis of high-resolution sulfidization profiles from a 30 m long sediment core (MD161/29) collected from the upper portion of the middle fan (west of SoNG) (Figure 1). The present study suggests a characteristic nature of sulfidization in Bengal fan sediments and its potential as a large sink of sulfide-sulfur. The findings are expected to throw light on the role of turbidite fan sedimentation in the global sulfur-carbon-iron biogeochemical cycle, an aspect not well recognized so far.

2. Materials and Method

2.1. Sub-bottom profiling and coring operation

Sub-Bottom Profiler (SBP) data acquired using a Seafalcon 11 echosounder onboard ORV *Marion Dufresne* (May, 2007). The central frequency used in this system was 3.75 kHz. This system produces high-resolution, zero-offset acoustic sections of the sub-surface as a function of the geographical position of the ship. The channel-levee complex was studied using SBP data. A 30 m long sediment core (MD 161/29: $17^{\circ} 18.04' \text{ N}$ latitude and $87^{\circ} 22.56' \text{ E}$ longitude) was collected from the levee portion of the channel-levee complex from a water depth of 2434m with a Giant Calypso piston corer. The core was sub-sampled into 5 cm slabs under N_2 shower and stored at 4°C for further analyses.

2.2. Multi-sensor core logging

The wet bulk density (WBD) and magnetic susceptibility (MS) of the whole core were measured onboard using GEOTEK multi-sensor core logger (MSCL) following equilibration of the core to the room temperature. The WBD was measured by gamma attenuation technique using Cs-137 as a gamma source and a detector comprising of a NaI(Tl) crystal scintillator and a photomultiplier tube. A standard aluminum rod with varying diameter was used for calibrating the gamma sensor. The MS was measured bypassing the core through the Bartington loop sensor (MS2C) on whole cores. The MS sensor was calibrated electronically using a standard sample of a stable iron oxide material.

2.3. Grain size determination

Microtrac S3500 Laser Particle Size Analyser was used for grain size determination. Freeze-dried sediment samples were desalinated, decarbonated (1N HCl) and H_2O_2 treated for the removal of sea-salts, inorganic carbonates, and organic matter respectively. The sample suspensions were

decoagulated and ultrasonicated before introduction to the laser path using the auto-sequence function provided in the Microtrac software.

2.4. Radiocarbon age determination

The sediment core was age dated using AMS ^{14}C ages generated at the National Ocean Sciences AMS (NOSAMS) facility, Woods Hole Oceanographic Institution, USA. Dates were determined using planktonic foraminifera dominantly of the species *Globigerinoides ruber* and *Globigerinoides sacculifer*. Carbon dioxide generated from these foraminifera shells was converted to graphite over a catalyst. Graphite was pressed into targets and analyzed on the accelerator along with standards and process blanks. Two primary standards used during ^{14}C measurements are NBS Oxalic Acid I (NIST-SRM-4990) and Oxalic Acid II (NIST-SRM-4990C).

2.5 Sulfur speciation and isotope ratios

Elemental sulfur (S^0) was extracted (Azarova et al., 2001) following ~12 hr long shaking of freeze-dried sediment samples in HPLC grade acetone (Sigma Aldrich). The supernatant (centrifuged) containing S^0 was quantified on an HPLC (Waters 2489: UV/visible detector) using the C18 column by injecting 20 μl of solution. Acid volatile sulfur (AVS) and chromium reducible sulfur (CRS) were extracted sequentially with cold 6N HCl and boiling 1M CrCl_2 in 6N HCl solution respectively under oxygen-free environment following (Canfield et al., 1986; Mazumdar et al., 2012). The evolved H_2S was precipitated as Ag_2S for quantification of CRS & AVS and S-isotope ratio determination. The total reducible sulfur (TRIS) is presented as:

$$\text{TRIS} = \text{CRS} + \text{AVS} + \text{S}^0 \quad (\text{Eq.1})$$

$\delta^{34}\text{S}$ of AVS and CRS were measured on Thermo Delta-Vplus Isotope Ratio Mass Spectrometer in continuous flow mode coupled with an Elemental Analyzer (Thermo EA1112). Sulfur isotope ratios are reported in the standard delta notation as permil deviations from the VCDT (Vienna Canyon Diablo Troilite) with reproducibility better than $\pm 0.3\text{‰}$. IAEA standards SO-5, SO-6, S-1, and S-2 were used for the preparation of calibration curves.

2.6. Carbon, Nitrogen and iron analyses

Total inorganic carbon (TIC) contents were determined on UIC carbon coulometer (UIC CM5130), while total carbon (TC) and total nitrogen (TN) contents were analyzed on the elemental analyzer (Thermo Flash2000). 2,4-DNP was used as a calibration standard for TC and TN contents. TIC content of standard reference material (Ultrapure CaCO_3 from Sigma-Aldrich) was $12 \pm 0.25\text{‰}$. The total organic carbon (TOC wt%) was measured by subtracting TIC from TC contents.

The carbon isotope ratio of total organic carbon ($\delta^{13}\text{C}_{\text{TOC}}$) was measured on decarbonated sediments using a Delta-V-plus isotope ratio mass spectrometer coupled with an elemental analyzer (Thermo EA1112). The external standard reproducibility calculated for $\delta^{13}\text{C}_{\text{TOC}}$ is typically 0.07‰ (VPDB).

Dithionite leachable iron (Fe_D :ferrihydrite, akageneite, lepidocrocite, goethite and hematite, and Fe-monosulfide (ref)) which represents highly reactive iron in the sediments was extracted with citrate buffered sodium dithionite (CBD) solution following Mehra and Jackson(1960), Canfield(1989) and Poulton and Canfield (2005). The extracted iron was measured by ferrozine-complexometry on a Chemito spectrophotometer (Spectroscan UV 2700). Absorbance was measured at 515 nm. Poulton and Canfield (2005) reported only minor (~5.6 %) removal of sedimentary magnetite using CBD solution. Since Fe_D also includes Fe_{AVS} , the latter was subtracted from the Fe_D to calculate the Fe_{ox} content (Yucel et al., 2010a) which represents the highly reactive Fe-oxides other than magnetite. For the extraction of sedimentary magnetite iron (Fe_{Mag}), CBD treated residual sediment was leached with 0.2 M ammonium oxalate of 3.2 pH for 6 h (Poulton and Canfield, 2005). Iron concentration in the leachate was measured on an Atomic Absorption Spectrophotometer (Agilent: 200 Series AA). The calibration line was prepared using Fluka iron standard for AAS. Standard reproducibility for Fe concentration measurement is 0.3%. Total reactive iron (Fe_{TR}) content is expressed (Eq. 2) as the sum of the pyrite-bound iron (Fe_{CRS}), dithionite (Fe_D) and oxalate extractable iron (Fe_{Mag}).

$$\text{Fe}_{\text{TR}} = \text{Fe}_{\text{CRS}} + \text{Fe}_D + \text{Fe}_{\text{Mag}} \quad (\text{Eq.2})$$

3. Results

3.1. Sub-bottom profiler data and core description

The SBP data (Figure 2) reveals undulating seafloor on either side of the coring location. High amplitude, parallel continuous reflections are observed in the upper 16 mbsf. Below this depth, multiple acoustically transparent layers (~0.3 to 3 m) are observed. The SBP image suggests the recurrence of thick acoustically transparent layers below the coring depth (30 mbsf).

The top 16 m of the core MD161/29 is olive green in color (Figure 2A). The sediment color changes to black below the greyish transition zone (16 to 17 mbsf). The sediments below 29 mbsf are greyish. Wet bulk density (Figure 3C) and MS (Figure 3D) show marked enhancement within 17-23 mbsf. MS data show multiple spikes throughout the core, however, a maximum number of MS spikes are recorded below 16 mbsf (Supplementary Table 1).

3.2. Age dating and grain size distribution

The core top age in MD161/29 is 1486 y BP, whereas, the maximum measured age (47,616 y BP; Supplementary material Table-2) is recorded at a depth of ~17.5 mbsf. The age-depth profile (Figure 3A) shows variability in sedimentation rate ranging from 19 to 243 cm/ky (Supplementary Figure-1) with an average sedimentation rate of 38.8 cm/ky (Figure 3A).

The silt (2- 63 μm)and clay (<2 μm) size fractions range from 83.7 to 96.1 vol% (avg.: 90.4 \pm 2.1 vol%) and 1.5-15 vol% (avg.: 8.3 \pm 2 vol%) respectively. The D_{50} values (median grain size: Supplementary material Table 3) range from 4.8 to 22.4 μm (Figure 3B).

3.3 CaCO₃ and organic C and total N content

The CaCO₃ content (Figure 3E; Supplementary material Table-4) ranges from (3.3 to 11.3 wt%) above 15 mbsf. Below this depth, CaCO₃ content ranges from 2-5 wt%. Microscopic observations suggest the occurrence of dominantly pulverized calcareous shells below 15 mbsf. The TOC content (Figure 3F) ranges from 0.25 to 1.48 wt% (avg. = 0.53 \pm 0.12 wt%). The (TOC/TN)_{molar} content range from 6 to 20.6 (Supplementary Figure 2 and Supplementary Table 4). The $\delta^{13}\text{C}_{\text{TOC}}$ values range from -21.8 to -17.9‰ VPDB (Supplementary material Figure 2and Table 4).

3.4. Sulfur speciation and isotope ratios

Acid volatile sulfur could be detected and quantified only below 18.2 mbsf (Figure 4A; Supplementary Table-5). AVS content ranges from 0.001 to 0.63 wt% with maxima at ~23 (22.97) mbsf. CRS could be quantified throughout the core(Figure 4B; Supplementary Table-5). Based on the CRS contents three depth zones can be demarcatedin figure-4b. In the top 5.3 mbsf, the CRS content remains low (0.001 to 0.01 wt %). Within 5.3-17.5 mbsf, CRS content increases to a maximum value of 0.16 wt% at a depth of 14.9 mbsf followed a sharp drop to 0.012 wt% at a depth of 17.5 mbsf. The third zone ranges from 18 to 30 mbsf where the CRS content fluctuates between 0.004 and 0.29 wt%. The S⁰ is also quantified (Figure 4C) primarily below 18.2 mbsf barring few peaks within the 12 to 17 mbsf.The S⁰ content ranges from negligible to 0.25 wt%. The total reducible sulfur (TRIS = CRS+AVS+S⁰) ranges from 0.001 to 0.88 wt% (Figure 4D). The TRIS content shows marked enhancement within 17 to 30 mbsf.The Fe_{CRS}, Fe_{AVS},Fe_{Mag}, , Fe_D, Fe_{Ox}, and Fe_{TR}contents range 0.001 to 0.25 wt%, 0.002 to 1.1 wt%, 0.05 to 1.31 wt%, 0.38 to 1.43 wt %, 0.048 to 1.39 and 0.7 to 2.7 wt% respectively (Supplementary Table-5). Compared to Fe_{TR}, the Fe_{Ox} profile shows marked enrichment within the turbidite dominatedzone (Figure 4E).

$\delta^{34}\text{S}_{\text{AVS}}$ values increase down the core depth (below 18.3 mbsf) with marked fluctuations (Figure 4A). The isotope ratios range from -36.6 to +64.4 ‰. In comparison to the CRS contents, $\delta^{34}\text{S}_{\text{CRS}}$ profile (Figure 4B) can be divided into three zones. The top 5.3 mbsf shows upward ^{34}S enrichment from $\delta^{34}\text{S}_{\text{CRS}}$ values ranging from -47.6 to 2.8 ‰ with intermittent peaks with positive excursions. Within 5 to 17.5 mbsf, the $\delta^{34}\text{S}_{\text{CRS}}$ values remain mostly within -30 to -50‰ barring a few high values. Below 17.5 mbsf, the $\delta^{34}\text{S}_{\text{CRS}}$ values increase with depth (-43.7 to +39 ‰) with multiple ^{34}S enrichment peaks. The $\delta^{34}\text{S}_{\text{AVS}}$ and $\delta^{34}\text{S}_{\text{CRS}}$ cross plot shows an excellent positive correlation ($r^2 = 0.85$; Figure 5). The analytical data are presented in the supplementary material table 5. The distribution of CRS, AVS contents, $\delta^{34}\text{S}_{\text{AVS}}$, and $\delta^{34}\text{S}_{\text{CRS}}$ are values presented as a histogram (Supplementary Figure 3A-D) showing marked variations between turbidite and hemipelagic dominated sequences.

4. Discussion and Conclusions

4.1 Hemipelagic and turbidite facies

Two distinct reflection patterns (high amplitude and acoustically transparent) are observed in the SBP data (Figure 2). The high amplitude reflection (dark color) approximately in the top 16-17 mbsf is attributed to the variation in acoustic impedance (density \times acoustic velocity) caused primarily by the fluctuations in WBD. In deep-sea sediments, the WBD is primarily controlled by the variability in calcium carbonate content (Figure 3E) while the acoustic velocity changes are almost negligible (Mayer, 1979). The large contrast in acoustic impedance results in high amplitude reflection. In contrast, the acoustically transparent layers represent reduced variation in interlayer acoustic properties due to rapid deposition (mass transport: Damuth, 1980) caused by channel spilling and low variability in calcium carbonate content (Figure 3E). The high amplitude reflection (dark color) and the acoustically transparent package indicate hemipelagic and turbidite rich sedimentary facies respectively (Figure 2).

The physically discernible clay-silt turbidite beds are demarcated with green colored bands (Figure 3) based on enhanced MS, WBD and D_{50} values (France-Lenord et al., 2016; Kuwae et al., 2013; Weber et al., 2003). The D_{50} data suggest the dominance of fine-medium silt size fraction. The turbidite dominated zone is enriched in detrital muscovite mica flakes (>63 µfractions), fine quartz, and iron oxide grains (marked in Figure 3E). Similar mineralogical and D_{50} data characteristics have also been reported by Fauquembergue et al. (2019) and Fournier et al. (2017) from the middle Bengal Fan. The enhanced MS values are correlatable with the D_{50} and WBD in most of the turbidite dominated zone. However, compared to the sand turbidite beds, the correlation of these physical

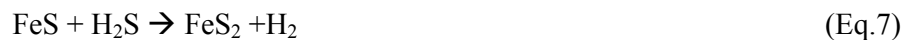
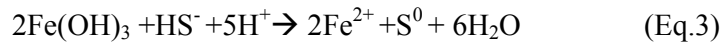
parameters is less obvious in clay-silt turbidite in Bengal fan (Weber et al., 2003). The MS spikes are commonly attributed to a higher concentration of magnetite, which may be present at the base of turbidite sequences because of higher magnetite's grain density than average grain density (Thompson & Oldfield, 1986). Although the presence of greigite (as a component of AVS) and the possible influence on the MS values cannot be ruled out, the absence of covariance of MS and AVS profiles (Figures 4D and 4A) negates the possibility of any dominant influence of AVS on the MS values. The thickest turbidite layers occur within 16 and 21 mbsf, followed downwards by multiple thinner turbidite layers (Figures 2 and 3). Multiple thin turbidite layers are observed within hemipelagic facies. The three distinct MS spikes recorded within the top 16 mbsf (dominantly hemipelagic sediments: Figure 3) show no concomitant enhancement in WBD and D_{50} grain sizes. On the other hand, these spikes are associated with CaCO_3 enrichment. The CaCO_3 contents in the turbidite dominated facies are lower than that of the hemipelagic dominated facies (Figure 3E). The relatively lower CaCO_3 (fragmented/pulverized foraminifera) content in the turbidite rich sequence may be attributed to dilution caused by high sedimentation rate of turbidite layers (Dennielou et al., 2006). The CaCO_3 profile through the turbidite and hemipelagic dominated zones observed in our study is very similar to the previously reported data from the Bengal Fan (Weber et al., 2003). Compared to the fragmented/pulverized foraminifera shells in the turbidite rich zone, the hemipelagic rich zone is enriched in well-preserved foraminifera shells, similar observations are also earlier reported by Fauquembergue et al. (2019). The $(\text{TOC}/\text{TN})_{\text{molar}}$ ratio and $\delta^{13}\text{C}_{\text{TOC}}$ (Supplementary Figure 2) suggest the contribution of both marine and terrestrial organic load with a variable mixture of C3 and C4 type vegetation (Galy et al., 2008) as the organic matter source in the Bengal Fan sediments.

Although the sedimentation rate could not be measured below 17.5 mbsf, it may be expected to be markedly higher than the overlying hemipelagic deposits. Recently, Fournier et al. (2017) reported sedimentation rates of ~4000 to 9000 cm/ky from the Bengal fan clay-silt turbidites in a core MD12-3417 (Figure 1) collected close to the active channel (~110 km from MD161/29). Fournier et al. (2017) and Weber et al. (1997) reported sedimentation rate only for the Holocene turbidite deposits which cannot directly be compared with much older (>47 ky) turbidites from MD161/29. The radiocarbon-based age dating (Figure 3A) suggests that the turbidite dominated sedimentary package deposited before 47 ky BP. The turbidite sedimentation indicates enhanced channel activity triggered either by tectonic processes or climatic changes including sea-level drop and/or monsoon-driven increase in fluvial flux (Schwenk, and Spieß, 2009; Fournier et al., 2017; Weber and Reilly, 2018). Since the presently active channel is supposed to have initiated ~ 14.5 ky BP (Weber et al., 1997; Hubscher et al., 1997), the intense turbidity flow observed in the present

study (>47 ky BP) is attributed to paleo-channel activity before 14.5 ky BP. The waning of the turbidity flow resulted in the predominance of hemipelagic sediments with an average sedimentation rate of 38.8 cm/ky.

4.2 Contrasting sulfidization

The hemipelagic and the turbidite sedimentary packages show remarkable contrast in the nature of sulfidization (Figure 4). One of the most striking observations in this study is the focused accumulation of AVS (Fe-monosulfide) and S⁰ within the turbidite dominated facies (Figure 4A &C). The black color of the sediment within the turbidite zone may be attributed to FeS precipitation. CRS which primarily represents FeS₂ is quantifiable in the hemipelagic facies as well (Figure 4B). The TRIS contents (Figure 4D) in the turbidite rich sediments are markedly higher as compared to that of hemipelagic sediments. FeS being the precursor of FeS₂, the relative contents of the two sulfide phases (FeS & FeS₂) depend on the extent of conversion of FeS to FeS₂ via H₂S and/or polysulfide pathways (Eqs. 3-7: Butler et al., 2004; Rickard and Luther III, 2007; Yucel et al., 2010a). The polysulfide pathway is the dominant pathway at porewater pH >7, whereas, H₂S pathway dominates at lower pH. Conversion of FeS to FeS₂ via H₂S pathway has been suggested to be mediated by microbial processes and energy metabolism (Thiel et al., 2019). The polysulfide pathway is kinetically much slower ($8 \times 10^{-11} \text{ mol l}^{-1} \text{s}^{-1}$) compared to the H₂S pathway ($2 \times 10^{-8} \text{ mol l}^{-1} \text{s}^{-1}$). Enrichment of FeS and S⁰ within the turbidite dominated zone suggest the possible significance of the polysulfide pathway (Rickard and Luther III, 2007).



The focusing of FeS and S⁰ in the turbidite dominated facies and their preservation may be attributed to partial pyritization of FeS due to H₂S/HS⁻ limitation relative to reactive iron content (Jørgensen et al., 2004; Riedinger and Brunner, 2014, 2017). Under high sedimentation rate conditions, conversion of FeS to FeS₂ (via Eq.5 to 7) would be hindered owing to the diminished exposure time of FeS to H₂S/HS⁻ rich zone as well as the reduced synthesis of sulfur intermediate (polysulfide) at the redox boundary (Hurtgen et al., 1999; Kraal et al., 2013). Although

Fe_{TR} content does not show any major shift within the turbidite rich facies, the Fe_{Ox} content is markedly enhanced within this zone (Figure 4E) supporting $\text{H}_2\text{S}/\text{HS}^-$ limitation relative to reactive iron content(Yucel et al., 2010a).Rapid sedimentation of clay-silt turbidite is expected to cut off the downward flux of oxygen by markedly reducing bioturbation (Wetzel and Wijayananda, 1990). Diminishedoxidative respiration of organic matter leads to enhanced burial of labile organic molecules (Arndt et al., 2013; Burdige, 2007)which promotes high sulfate reduction rate(Bowles et al, 2014; Beulig et al, 2018; Canfield, 1989, Canfield,1994; Jørgensen et al., 2019). The sharp down-depth depletion of pore-water SO_4^{2-} concentrations (microbial sulfate reduction) and consequent formation of H_2S rich zone (Riedinger et al., 2005; Riedinger et al., 2017)is driven by organo-clastic and/orAOM pathways (Egger et al., 2016; Knittel and Boetius, 2009; Jørgensenand Kasten, 2006;Reeburgh, 2007)represented by overalleguations 8 and 9.



In contrast to the turbidite rich zone, the slowly depositing hemipelagic sediments likely experienced extensive bioturbation (Wetzel and Wijayananda, 1990) causingmicrobially driven oxidative recycling of H_2S which may lead to the well-recognized disproportionation of sulfide intermediates like S^0 , SO_3^{2-} and $\text{S}_2\text{O}_3^{2-}$ (Canfield and Thamdrup,1994;Jorgenesen, 1990). The non-detectable AVScontent and scant occurrences of S^0 in the hemipelagic zone suggest the possibility oftwo different scenarios/settingslike (a) efficient consumption of AVS and S^0 through pyritization and subsequent burial below the apparent redox potential discontinuity depth (aRPD) layer (Gerwing et al., 2015) and/or (b) pyritization following ‘ferric-hydroxide-surface (FHS)FHS pathway suggestedby Wan et al.(2017) where high pyritization may be possible without buildup of intermediate FeSat high Fe(III):S(-II) ratios.The key speciescontrolling the overall pyrite formation mechanism appearsto be $>\text{Fe}^{\text{II}}\text{OH}_2^+$, i.e. ferrous iron forming at the mineralsurface upon sulfidation of ferric hydroxides.Near-surface oxidation of H_2S may lead to high Fe(III):S(-II) conditions under the aerobic depositional realm.

The plausible biogeochemical pathways (Eqs.3-7) stated aboveare further supported by the CRS/AVS sulfur isotope ratios. The $\delta^{34}\text{S}_{\text{AVS}}$ values(-36.6 to +64.4‰) increase down the core depth (below 18.3 mbsf) superimposed by marked ^{34}S enrichment peaks. The sharp spikes in the isotope ratios ($\delta^{34}\text{S}_{\text{AVS}}$) suggest rapid consumption of pore-water SO_4^{2-} via microbially mediated sulfate reduction in a closed system conditions created by turbidite deposits(Berelson et al., 2019; Claypool et al., 2004; Liu et al., 2019; Shaw and Meyers, 1996) leading to pore water SO_4^{2-} limitation and

subsequent ^{34}S enrichment of dissolved HS^- due to Rayleigh fractionation (Canfield, 2001). It is also important to mention that individual turbidite flow is also characterized by basal erosion exposing isotopically enriched H_2S to the reactive iron in the overlying turbidite layer leading to the precipitation of AVS with high $\delta^{34}\text{S}$ values (Aller et al., 2010; Fike et al., 2015). Infact, figure 4E show high reactive Fe_{Ox} content in the turbidite layers. The above process may also be responsible for the dominance of sulfidization towards the base of the turbidite layers. The input of fresh organic matter with each turbidite pulse would also enhance the sulfate reduction rate and ^{34}S enrichment (Burdige, 2006).It is important to note that ^{34}S depleted AVS/CRS occurs mostly in between the turbidite beds characterized by hemipelagic intervals. However, deviations from this observation may be attributed to the diffusion of H_2S across the depositional boundaries. A higher resolution sampling is required for the precisecorrelationof the turbidite/ hemipelagic couplets with the S-isotopic ratios in Fe-sulfide phases.The systematic increase in the background $\delta^{34}\text{S}_{\text{AVS}}$ and $\delta^{34}\text{S}_{\text{CRS}}$ may be attributed to the superimposition of a down-core gradient in the isotopic composition of sulfide phases that are enriched as the result of progressively closed system properties.The rapid depositional phases of individual turbidite beds and rapid vertical buildup of the total package are responsible for the development of sharp individual ^{34}S enrichment spikes and typical down-depth ^{34}S enrichment gradient respectively. The contrasting down core gradient of $\delta^{34}\text{S}_{\text{CRS}}$ from hemipelagic to turbidite facies may be attributed to enhanced sedimentation rateand its influence on sulfate reduction rate as explained above.The $\delta^{34}\text{S}_{\text{CRS}}$ values show a remarkablepositive correlation ($r^2 = 0.85$) with $\delta^{34}\text{S}_{\text{AVS}}$ (Figure 5) suggesting AVS as the likely precursor for the CRS synthesis via pathways represented by equations6.. The large $\delta^{34}\text{S}_{\text{CRS}}$ range (-43.7 to +39 %) observed within the turbidites dominated zone has equivalence form the turbidite beds off Nankai trough (IODP 316; Riedinger and Brunner, 2014).

The $\delta^{34}\text{S}_{\text{CRS}}$ profile in the hemipelagic dominated zone reflects early diagenetic pyritization close to the sediment-water interface where steady diffusive and/or advective (bioturbation) sulfate flux prevented sulfate limitation and ^{34}S enrichment. Enhanced bioturbation activity and deeper oxidative processes in the hemipelagic succession may be attributed to a possible drastic drop in sedimentation rate relative to the underlying turbidite dominated zone. The consistently ^{34}S depletedCRS values ($\delta^{34}\text{S}_{\text{CRS}}$ ranging from -30 to -50‰) recorded within the 5 to 17.5 mbsf suggest S-isotopic fractionation of 56 to 70 ‰ relative to the average seawater sulfate sulfur isotope ratio (~ +21‰:Rees et al., 1978) which is markedly within the range of reported fractionation of 5 to 70‰ measured for the natural environment and laboratory cultures involvingdirect dissimilatory sulfate reduction pathways(Brunner and Bernasconi, 2005; Canfield and Teske, 1996; Habicht and Canfield,

1996; Colangelo-Lillis et al., 2019; Leavitt et al., 2013; Sim et al., 2011; Wing and Halevy, 2014; Wortmann et al., 2001). Recent finding by Sim et al. (2019) suggests marked influence of electron donor availability (simple organic molecule & H₂) on the reversibility of adenosinephosphosulfate reductase (Apr) driven reaction on large sulfur isotopic fractionation. In addition to direct dissimilatory sulfate reduction pathways, the disproportionation of sulfur intermediates like S⁰, SO₃²⁻ and S₂O₃²⁻ produced during the oxidative part of the sulfur cycle may be invoked (Canfield and Thamdrup, 1994; Jørgensen, 1990; Jørgensen et al. 2019) to explain the observed large S-isotopic fractionation. Within the top 17.5 mbsf, multiple positive S-isotopic excursions (11.3 to 39.3 ‰) are observed. Such positive excursions in δ³⁴S_{CRS} values have commonly been attributed to episodes of high sedimentation rates since rapid sedimentation episode is expected to create closed diagenetic system leading to ³⁴S enrichment of residual SO₄/ H₂S (Berelson et al., 2019; Claypool ., 2004; Liu et al., 2019; Pasquier et al., 2017). Although in the present study, sedimentation rate profile (Supplementary Figure-1A) shows enhanced rates including the 14-15 ky BP event correlated with the channel activation around 14.5 ky BP (Weber et al., 1997; Fournier et al., 2017; Fauquembergue et al., 2019), only a partial coherence could be observed between the positive S-isotope excursions and enhanced sedimentation rates (Supplementary material Figure 1). A partial match of the sedimentation rate profile and ³⁴S enrichment zone possibly suggests the influence of additional factors like diminished bioturbation activity which can also lead to a closed diagenetic system and diffusion of Fe²⁺ and H₂S across the depositional layers responsible for the ³⁴S profiles (Passier et al., 1996).

CRS contents (0.001 to 0.013 wt%) sharply drop in the top 5 mbsf (Figure 4B). This zone shows an overall ³⁴S enrichment trend (-46.7 to +2.8 ‰ VCDT) towards the sediment-water interface. Sharp lowering of CRS contents coupled with an overall increasing trend in δ³⁴S_{CRS} values towards the sediment-water interface defines a redox front ~ 5 m bsf. Similar trends in CRS contents and δ³⁴S_{CRS} ratios at variable depth bsf have earlier been reported by Aller et al. (2010); Borowski et al. (2013), Raven et al., (2016) and Dale et al., (2009). Aller et al. (2010) and Fike et al. (2015) attributed the ³⁴S enrichment of CRS towards the sediment-water interface to the existence of mobile, reactive Fe-rich suboxic sediment layer over a stable anoxic layer. Apparently, the sulfidization of reactive iron in the recycled overlying layer by ³⁴S-enriched H₂S diffusing from the underlying stable layer results in ³⁴S enriched CRS in the mobile layer. However, this pathway is unlikely in the case of MD161/29, because such recycling is expected to result in the sediment homogenization of top 5 mbsf, which is not supported by a steady increase in sediment age with depth (Figure 3A). Moreover, such recycling is suggested as a dominant process in the deltaic inner shelf depositional settings and

not in the deep seas (Aller et al., 2010). The low CRS contents may be attributed to the re-oxidation of H₂S and Fe-monosulfide via nitrate reduction (Dale et al., 2009) and MnO₂ pathways (Schippers and Jørgensen, 2002). The marked ³⁴S enrichment in CRS may be attributed to a complex and repetitive microbially mediated cycling of sulfate reduction and sulfide oxidation (Fry et al., 1988; Dale et al 2009).

Our observations have drawn a clear distinction between hemipelagic and turbidite sedimentation in terms of sedimentary sulfidization and S-isotopic composition. The role of enhanced sulfur burial in turbidite fan sedimentation (Otero et al., 2003; Riedinger and Brunner, 2014; Shaw & Meyers, 1996; Taillefert et al., 2017; Yucel et al., 2010a and 2010b) may have remarkable implication in global Fe-C-Scycle. Given the enormous area, thickness and numerous cycles of channel-levee distribution over the geologic time, the Bengal fan sediments can be considered as a globally significant iron-sulfur sink coupled with the high organic loading. The present study opens up the window for further investigation on other channel-levee fan systems for better understanding and quantification of the marine Fe-S-C cycle.

Acknowledgments, Samples, and Data

We thank the directors of CSIR-NIO, NIOT, NCPOR, and Secretary, Ministry of Earth Sciences(Govt. of India) for supporting this study. Sincere thanks to students of Goa University, IIT Kharagpur and project scientists of CSIR-NIO, NIOT, PRL, and CSIR-NGRI. We are grateful for the comments and suggestions from NIO-publication committee for suggestions to improve the manuscript. There are no real or perceived financial conflicts of interests for any author. There is no conflict of interest with respect to the results of this paper. Complete data set is included in the manuscript as supplementary tables. The program was funded by Ministry of Earth Sciences(Govt. of India). **Complete data set is included in the manuscript as supplementary tables. We will upload the data at the relevant site once the manuscript is accepted.**

References

- Aller, R. C., Madrid, V., Chistoserdov, A., Aller, J. Y., & Heilbrun, C. (2010). Unsteady diagenetic processes and sulfur biogeochemistry in tropical deltaic muds: implications for oceanic isotope cycles and the sedimentary record. *Geochimica et Cosmochimica Acta*, 74(16), 4671-4692. DOI : 10.1016/j.gca.2010.05.008
- Anschutz, P., Jorissen, F. J., Chaillou, G., Abu-Zied, R., & Fontanier, C. (2002). Recent turbidite deposition in the eastern Atlantic: early diagenesis and biotic recovery. *Journal of Marine Research*, 60(6), 835-854. <https://doi.org/10.1357/002224002321505156>
- Arndt, S., Jørgensen, B. B., LaRowe, D. E., Middelburg, J. J., Pancost, R. D., & Regnier, P. (2013). Quantifying the degradation of organic matter in marine sediments: a review and synthesis. *Earth-science reviews*, 123, 53-86. <https://doi.org/10.1016/j.earscirev.2013.02.008>
- Azarova, I. N., Gorshkov, A. G., Grachev, M. A., Korzhova, E. N., & Smagunova, A. N. (2001). Determination of elemental sulfur in bottom sediments using high-performance liquid chromatography. *Journal of Analytical Chemistry*, 56(10), 929-933. <https://doi.org/10.1023/A:1012309411889>
- Berelson, W.M., Morine, L., Sessions, A., Rollins, N., Fleming, J. C., & Schwalbach, J. (2019). Santa Barbara Basin Flood Layers: Impact on Sediment Diagenesis. In: Mountains to the Abyss: The California Borderland as an Archive of Southern California Geologic Evolution, *SEPM special issue*, 110, 233-240. Doi: 10.2110/sepmse.110.11.
- Beulig, F., Røy, H., Glombitza, C., & Jørgensen, B.B., (2018). Control on rate and pathway of anaerobic organic carbon degradation in the seabed. *Proc. Natl. Acad. Sci. U.S.A.* 115, 367-372. <https://doi.org/10.1073/pnas.1715789115>
- Borowski, W. S., Rodriguez, N. M., Paull, C. K., & Ussler III, W. (2013). Are 34S-enriched authigenic sulfide minerals a proxy for elevated methane flux and gas hydrates in the geologic record?. *Marine and Petroleum Geology*, 43, 381-395.
- Bowles, M.W., Mogollón, J.M., Kasten, S., Zabel, M., & Hinrichs, K.U. (2014). Global rates of marine sulfate reduction and implications for sub-sea-floor metabolic activities. *Science* 344, 889-891. doi: 10.1126/science.1249213
- Butler, I. B., Böttcher, M. E., Rickard, D., & Oldroyd, A. (2004). Sulfur isotope partitioning during experimental formation of pyrite via the polysulfide and hydrogen sulfide pathways: implications for the interpretation of sedimentary and hydrothermal pyrite isotope records. *Earth and Planetary Science Letters*, 228(3-4), 495-509. <https://doi.org/10.1016/j.epsl.2004.10.005>
- Burdige, D.J. (2006). *Geochemistry of marine sediments*. Princeton University Press, pp. 609
- Brunner, B., & Bernasconi, S.M. (2005). A revised isotope fractionation model for dissimilatory sulfate reduction in sulfate reducing bacteria. *Geochimica et Cosmochimica Acta* 69, 4759-4771. <https://doi.org/10.1016/j.gca.2005.04.015>
- Burdige, D. J. (2007). Preservation of organic matter in marine sediments: controls, mechanisms and an imbalance in sediment organic carbon budgets? *Chem. Rev.* 107, 467–485. <https://doi.org/10.1021/cr050347q>

Canfield, D. E., Raiswell, R& Westrich J. (1986). The use of chromium reduction in the analysis of reduced inorganic sulphur in sediments and shales, *Chemical Geology*, 54, 149-155. [https://doi.org/10.1016/0009-2541\(86\)90078-1](https://doi.org/10.1016/0009-2541(86)90078-1)

Canfield, D. E. (1989). Sulfate reduction and oxic respiration in marine sediments: implications for organic carbon preservation in euxinic environments. *Deep-Sea. Res. PT. I* 36, 121–138. [https://doi.org/10.1016/0198-0149\(89\)90022-8](https://doi.org/10.1016/0198-0149(89)90022-8)

Canfield, D. E. (1994). Factors influencing organic carbon preservation in marine sediments. *Chemical Geology*, 114(3-4), 315-329. [https://doi.org/10.1016/0009-2541\(94\)90061-2](https://doi.org/10.1016/0009-2541(94)90061-2)

Canfield, D. E, & Thamdrup, B. (1994). The production of ^{34}S -depleted sulfide during bacterial disproportionation of elemental sulfur. *Science*, 266(5193), 1973-1975. <https://doi.org/10.1126/science.11540246>

Canfield, D. E. (2001). Biogeochemistry of sulfur isotopes. *Reviews in Mineralogy and Geochemistry*, 43(1), 607-636. <https://doi.org/10.2138/gsrmg.43.1.607>

Canfield, D. E, Kristensen, E. & Thamdrup, B. (2005). The sulfur cycle. *Advances in Marine Biology*, 48, 313-381. [https://doi.org/10.1016/S0065-2881\(05\)48009-8](https://doi.org/10.1016/S0065-2881(05)48009-8)

Canfield, D. E., & Teske, A. (1996). Late Proterozoic rise in atmospheric oxygen concentration inferred from phylogenetic and sulphur-isotope studies: *Nature*, v. 382, (10) 127–132. <https://doi.org/10.1038/382127a0>

Claypool, G. (2004). Ventilation of marine sediments indicated by depth profiles of pore water sulfate and $\delta^{34}\text{S}$, *The Geochemical Society Special Publications*, 9, 59-65. [https://doi.org/10.1016/S1873-9881\(04\)80007-5](https://doi.org/10.1016/S1873-9881(04)80007-5)

Clemens, S.C., Kuhnt, W., LeVay, L.J., Anand, P., Ando, T., Bartol, M., Bolton, C.T., Ding, X., Gariboldi, K., Giosan, L., Hathorne, E.C., Huang, Y., Jaiswal, P., Kim, S., Kirkpatrick, J.B., Littler, K., Marino, G., Martinez, P., Naik, D., Peketi, A., Phillips, S.C., Robinson, M.M., Romero, O.E., Sagar, N., Taladay, K.B., Taylor, S.N., Thirumalai, K., Uramoto, G., Usui, Y., Wang, J., Yamamoto, M., and Zhou, L., 2016. Site U1444. In Clemens, S.C., Kuhnt, W., LeVay, L.J., and the Expedition 353 Scientists, Indian Monsoon Rainfall. Proceedings of the International Ocean Discovery Program, 353: College Station, TX (International Ocean Discovery Program). <http://dx.doi.org/10.14379/iodp.proc.353.104.2016>

Colangelo-Lillis, J., Pelikan, C., Herbold, C. W., Altshuler, I., Loy, A., Whyte, L. G., & Wing, B. A. (2019). Diversity decoupled from sulfur isotope fractionation in a sulfate-reducing microbial community. *Geobiology*, 17(6), 660-675.

Curry, J. R. and Moore, D. G. (1971) Growth of the Bengal Deep Sea Fan and denudation in the Himalayas. *Bull. Geol. Soc. Am.*, 82, 562–572.

Curry, J. R., & Moore, D. G. (1974). Sedimentary and tectonic processes in the Bengal deep-sea fan and geosyncline, in *The geology of continental margins*, C.A. Burk and C.L. Drake (eds.), pp. 617-627, Springer. https://doi.org/10.1007/978-3-662-01141-6_45

Dale, A. W., Brückert, V., Alperin, M., & Regnier, P. (2009). An integrated sulfur isotope model for Namibian shelf sediments. *Geochimica et Cosmochimica Acta*, 73(7), 1924-1944.

- Damuth, J.E. (1980). Use of high-frequency (3.5–12 kHz) echograms in the study of near-bottom sedimentation processes in the deep-sea: a review. *Marine Geology*, 38(1-3), pp.51-75. [https://doi.org/10.1016/0025-3227\(80\)90051-1](https://doi.org/10.1016/0025-3227(80)90051-1)
- Dennielou, B., Huchon, A..Beaudouin, C. & Berne, S. (2006). Vertical grain-size variability within a turbidite levee: Autocyclicity or allocyclicity? A case study from the Rhone neofan, Gulf of Lions, Western Mediterranean, *Marine Geology*, 234(1-4), 191-213. <https://doi.org/10.1016/j.margeo.2006.09.019>
- Egger, M., Lenstra, W., Jong, D., Meysman, F.J., Sapart, C.J., van der Veen, C., Röckmann, T., Gonzalez, S., Slomp, C.P., 2016. Rapid sediment accumulation results in high methane effluxes from coastal sediments. *PLoS One* 11, e0161609.
- Einsele, G., Ratschbacher, L. & Wetzel, A. (1996). The Himalaya-Bengal Fan denudation-accumulation system during the past 20 Ma, *The Journal of Geology*, 104(2), 163-184. <https://www.jstor.org/stable/30064162>.
- Emmel, F. J., & Curran, J. R., (1983). The Bengal submarine fan, north-eastern Indian Ocean. *Geo-Mar. Lett.*, 3:119-12. <https://doi.org/10.1007/BF02462456>
- Fauquembergue, K., Fournier, L., Zaragosi, S., Bassinot, F., Kissel, C., Malaize, B., Caley, T., Moreno, E. & Bachelery, P. (2019). Factors controlling frequency of turbidites in the Bengal fan during the last 248 kyr cal BP: Clues from a presently inactive channel. *Marine Geology*, 415, 105965. <https://doi.org/10.1016/j.margeo.2019.105965>
- Fike, D. A., Bradley,A. S.& Rose, C. V. (2015), Rethinking the ancient sulfur cycle. *Annual Review of Earth and Planetary Sciences*, 43, 593-622.<https://doi.org/10.1146/annurev-earth-060313-054802>
- Fournier, L., Fauquembergue, K., Zaragosi, S., Zorzi, C., Malaizé, B., Bassinot, F., Joussain, R., Colin, C., Moreno, E. & Leparamentier, F. (2017). The Bengal fan: external controls on the Holocene Active Channel turbidite activity. *The Holocene*, 27(6), 900-913. <https://doi:10.1177/0959683616675938>
- France-Lanord, C., Derry,L. & Michard, A. (1993). Evolution of the Himalaya since Miocene time: isotopic and sedimentological evidence from the Bengal Fan. *Geological Society, London, Special Publications*, 74(1), 603-621. <https://doi.org/10.1144/GSL.SP.1993.074.01.40>
- France-Lanord, C., Spiess, V., Klaus, A., Schwenk, T., & the Expedition 354 Scientists (2016). Proceedings of the International Ocean Discovery ProgramVolume 354. doi: 10.14379/iodp.proc.354.103.2016.
- Fry, B., Ruf, W., Gest, H., & Hayes, J. M. (1988). Sulfur isotope effects associated with oxidation of sulfide by O₂ in aqueous solution. *Chemical Geology: Isotope Geoscience section*, 73(3), 205-210.
- Galy, V., France-Lanord, C., Beyssac, O., Faure, P., Kudrass, H. & Palhol, F. (2007), Efficient organic carbon burial in the Bengal fan sustained by the Himalayan erosional system. *Nature*, 450(7168), 407. doi:10.1038/nature06273

- Galy, V., François, L., France-Lanord, C., Faure, P., Kudrass, H., Palhol, F., & Singh, S. K. (2008). C4 plants decline in the Himalayan basin since the Last Glacial Maximum. *Quaternary Science Reviews*, 27(13-14), 1396-1409. <https://doi.org/10.1016/j.quascirev.2008.04.005>
- Gerwing, T. G., Gerwing, A. M. A., Hamilton, D. J., & Barbeau, M. A. (2015). Apparent redox potential discontinuity (aRPD) depth as a relative measure of sediment oxygen content and habitat quality. *International Journal of Sediment Research*, 30(1), 74-80. [https://doi.org/10.1016/S1001-6279\(15\)60008-7](https://doi.org/10.1016/S1001-6279(15)60008-7)
- Habicht, K., & Canfield, D. E. (1996). Sulphur isotope fractionation in modern microbial mats and the evolution of the sulphur cycle. *Nature*, 382, 342-343. [https://doi.org/10.1016/S0016-7037\(97\)00311-6](https://doi.org/10.1016/S0016-7037(97)00311-6)
- Hartnett, H. E., Keil, R. G., Hedges, J. I. & Devol, A. H. (1998). Influence of oxygen exposure time on organic carbon preservation in continental margin sediments. *Nature*, 391(6667), 572-574. <https://doi.org/10.1038/35351>
- Hubscher, C., Spieß, V., Breitzke, M. & Weber, M. E. (1997). The youngest channel-levee system of the Bengal Fan: Results from digital sediment echo sounder data. *Marine Geology*, 141(1-4), 125-145. [https://doi.org/10.1016/S0025-3227\(97\)00066-2](https://doi.org/10.1016/S0025-3227(97)00066-2)
- Hurtgen, M. T., Lyons, T. W., Ingall, E. D., & Cruse, A. M. (1999). Anomalous enrichments of iron monosulfide in euxinic marine sediments and the role of H₂S in iron sulfide transformations; examples from Effingham Inlet, Orca Basin, and the Black Sea. *American Journal of Science*, 299(7-9), 556-588. doi: 10.2475/ajs.299.7-9.556
- Jørgensen, B. B. (1990). A thiosulfate shunt in the sulfur cycle of marine sediments. *Science*, 249(4965), 152-154. DOI:10.1126/science.249.4965.152.
- Jørgensen, B. B., Böttcher, M. E., Lüschen, H., Neretin, L. N., & Volkov, I. I. (2004). Anaerobic methane oxidation and a deep H₂S sink generate isotopically heavy sulfides in Black Sea sediments. *Geochimica et Cosmochimica Acta*, 68(9), 2095-2118.
- Jørgensen, B. B., & Kasten, S. (2006). Sulfur cycling and methane oxidation, in *Marine geochemistry*, edited, pp. 271-309, Springer. https://doi.org/10.1007/3-540-32144-6_8
- Jørgensen, B. B., Findlay, A. J., & Pellerin, A. (2019). The Biogeochemical Sulfur Cycle of Marine Sediments. *Frontiers in microbiology*, 10. <https://doi.org/10.3389/fmicb.2019.00849>
- Knittel, K., & Boetius, A., (2009). Anaerobic oxidation of methane: progress with an unknown process. *Annu. Rev. Microbiol.* 63, 311–334. DOI: 10.1146/annurev.micro.61.080706.093130
- Kraal, P., Burton, E. D., & Bush, R. T. (2013). Iron monosulfide accumulation and pyrite formation in eutrophic estuarine sediments. *Geochimica et Cosmochimica Acta*, 122, 75-88. <https://doi.org/10.1016/j.gca.2013.08.013>
- Krishna, K. S., Ismaiel, M., Srinivas, K., Gopala Rao, D., Mishra, J. & Saha, D. (2016), Sediment pathways and emergence of Himalayan source material in the Bay of Bengal, *Current Science*, 110 (3), 363-372. <http://drs.nio.org/drs/handle/2264/4921>

- Kuwae, M., Yamamoto, M., Ikebara, K., Irino, T., Takemura, K., Sagawa, T., Sakamoto, T., Ikebara, M. & Takeoka, H. (2013). Stratigraphy and wiggle-matching-based age-depth model of late Holocene marine sediments in Beppu Bay, southwest Japan, *Journal of Asian Earth Sciences*, 69, 133-148. <https://doi.org/10.1016/j.jseaes.2012.07.002>
- Leavitt, W.D., Halevy, I., Bradley, A.S., and Johnston, D.T. (2013). Influence of sulfate reduction rates on the Phanerozoic sulfur isotope record. *Proc. Natl. Acad. Sci. U.S.A.* 110, 11244–11249. doi:10.1073/pnas.1218874110
- Liu, X., Fike, D., Li, A., Dong, J., Xu, F., Zhuang, G., Rendle-Bühring, R. & Wan, S. (2019). Pyrite sulfur isotopes constrained by sedimentation rates: Evidence from sediments on the East China Sea inner shelf since the late Pleistocene. *Chemical Geology*, 505, pp.66-75. <https://doi.org/10.1016/j.chemgeo.2018.12.014>.
- Mazumdar, A., Peketi, A., Joao, H., Dewangan, P., Borole, D. V., & Kocherla, M. (2012). Sulfidization in a shallow coastal depositional setting: Diagenetic and palaeoclimatic implications. *Chemical Geology*, 322, 68-78.
- Mayer, L.A., (1979). Deep sea carbonates: Acoustic, physical and stratigraphic properties. *Journal of Sedimentary Petrology*, 49 (3), 0819-0836. <https://doi.org/10.1306/212F785B-2B24-11D7-8648000102C1865D>
- Mehra, O., & Jackson, M. (1960). Iron oxide removal from soils and clays by a dithionite-citrate system buffered with sodium bicarbonate. *Clays and clay Minerals*, 7, 317-327. <https://doi.org/10.1016/j.gca.2013.08.013>
- Otero, X. L., Huerta-Diaz, M. A. & Macias, F. (2003). Influence of a turbidite deposit on the extent of pyritization of iron, manganese and trace metals in sediments from the Guaymas Basin, Gulf of California (Mexico). *Applied Geochemistry*, 18(8), 1149-1163. [https://doi.org/10.1016/S0883-2927\(02\)00190-7](https://doi.org/10.1016/S0883-2927(02)00190-7)
- Passier, H., Middelburg, J., van Os, B. & G. de Lange (1996), Diagenetic pyritisation under eastern Mediterranean sapropels caused by downward sulphide diffusion, *Geochimica et Cosmochimica Acta*, 60(5), 751-763. [https://doi.org/10.1016/0016-7037\(95\)00419-X](https://doi.org/10.1016/0016-7037(95)00419-X)
- Pasquier, V., Sansjofre, P., Rabineau, M., Revillon, S., Houghton, J. & Fike, D. A. (2017). Pyrite sulfur isotopes reveal glacial-interglacial environmental changes. *Proceedings of the National Academy of Sciences*, 114(23), 5941-5945.
- Peketi, A., Mazumdar, A., Pillutla, S.P.K., Patil, D.J., 2020. Influence of dual sulfate reduction pathways on pore-fluid chemistry and occurrences of methane hydrate in sediment cores (IODP-353) off Mahanadi basin, Bay of Bengal. *Geochemical Journal* 54, 1-11, <https://doi.org/10.2343/geochemj.2.0576>
- Poulton, S., & Canfield, D.E (2005). Development of a sequential extraction procedure for iron: implications for iron partitioning in continental derived particulates. *Chemical Geology*, 214(3-4), 209-221. <https://doi.org/10.1016/j.chemgeo.2004.09.003>
- Raven, M. R., Sessions, A. L., Fischer, W. W., & Adkins, J. F. (2016). Sedimentary pyrite $\delta^{34}\text{S}$ differs from porewater sulfide in Santa Barbara Basin: Proposed role of organic sulfur. *Geochimica et Cosmochimica Acta*, 186, 120-134.

- Rees, C., Jenkins, W. & Monter, J. (1978). The sulphur isotopic composition of ocean water sulphate. *Geochimica et Cosmochimica Acta*, 42(4), 377-381. [https://doi.org/10.1016/0016-7037\(78\)90268-5](https://doi.org/10.1016/0016-7037(78)90268-5)
- Reeburgh, W. S. (2007). Oceanic methane biogeochemistry, *Chemical reviews*, 107(2), 486-513. <https://doi.org/10.1021/cr050362v>
- Rickard, D., & Luther III, G.W. (2007). Chemistry of Iron Sulfides. *Chemical Reviews*, 107, 514–562. <https://doi.org/10.1021/cr0503658>
- Riedinger, N., Pfeifer, K., Kasten, S., Garming, J. F. L., Vogt, C. & Hensen, C. (2005). Diagenetic alteration of magnetic signals by anaerobic oxidation of methane related to a change in sedimentation rate, *Geochimica et Cosmochimica Acta*, 69(16), 4117-4126. doi: 10.1016/j.gca.2005.02.004
- Riedinger, N., & Brunner, B. (2014). Data report: Concentration and sulfur isotope composition of iron monosulfide and pyrite from sediments collected during IODP expedition 316, Nankai Trough, Japan, Proc. Integrated Ocean Drill. Program, 314–316, <https://doi:10.2204/iodp.proc.314315316.223.2014>
- Riedinger, N., Brunner, B., Krastel, S., Arnold, G.L., Wehrmann, L.M., Formolo, M.J., Beck, A., Bates, S.M., Henkel, S., Kasten, S. & Lyons, T.W. (2017). Sulfur cycling in an iron oxide-dominated, dynamic marine depositional system: the Argentine continental margin. *Frontiers in Earth Science*, 5, p.33. DOI: 10.3389/feart.2017.00033.
- Schippers, A., & Jørgensen, B. B. (2002). Biogeochemistry of pyrite and iron sulfide oxidation in marine sediments. *Geochimica et Cosmochimica Acta*, 66(1), 85-92.
- Schwenk, T., Spieß, V. , Breitzke, M. & Hubscher, C. (2005). The architecture and evolution of the Middle Bengal Fan in vicinity of the active channel-levee system imaged by high-resolution seismic data, *Marine and Petroleum Geology*, 22(5), 637-656. <https://doi.org/10.1016/j.marpetgeo.2005.01.007>.
- Schwenk, T., & Spieß, V. (2009). Architecture and stratigraphy of the Bengal Fan as response to tectonic and climate revealed from high-resolution seismic data, External Controls on Deep-Water Depositional Systems. *Special Publication-SEPM (Society of Sedimentary Geologists)*, 92, 107-131. <https://doi.org/10.2110/sepmsp.092.107>
- Shaw, T. J., & Meyers, P. A. (1996). The implications of turbidite-driven redox changes in sediments of the Iberia Abyssal Plain, paper presented at Proceedings of the Ocean Drilling Program, Scientific Results. <http://dx.doi.org/10.2973/odp.proc.sr.149.238.1996>
- Sim, M. S., Bosak, T. & Ono, S. (2011). Large Sulfur Isotope Fractionation Does Not Require Disproportionation, *Science*, 333(6038), 74-77. <https://doi: 10.1126/science.1205103>
- Sim, M. S., Ogata, H., Lubitz, W., Adkins, J. F., Sessions, A. L., Orphan, V. J., & McGlynn, S. E. (2019). Role of APS reductase in biogeochemical sulfur isotope fractionation. *Nature communications*, 10(1), 44.
- Singh, D.S. (2017). The Indian Rivers: Scientific and Socio-economic Aspects (Editors: Singh, Dhruv Sen), Springer Hydrogeology, p, 551. DOI 10.1007/978-981-10-2984-4

Subrahmanyam V, Krishna K. S, Ramana M. V, Murthy K. S.(2008) Marine geophysical investigations across the submarine canyon (Swatch-of-No-Ground), northern Bay of Bengal. *Current Science*, 94, 507-513.

Taillefert, M., Beckler, J. S., Cathalot, C., Michalopoulos, P., Corvaisier, R., Kiriazis, N., Caprais, J.-C. Pastor, L. & Rabouille, C. (2017). Early diagenesis in the sediments of the Congo deep-sea fan dominated by massive terrigenous deposits: Part II-Iron-sulfur coupling. *Deep Sea Research Part II: Topical Studies in Oceanography*, 142, 151-166. <https://doi.org/10.1016/j.dsr2.2017.06.009>

Thiel, J., Byrne, J. M., Kappler, A., Schink, B., & Pester, M. (2019). Pyrite formation from FeS and H₂S is mediated through microbial redox activity. *Proceedings of the National Academy of Sciences*, 116, 6897-6902. doi/10.1073/pnas.1814412116

Thompson, R. & Oldfield, F. (1986). Environmental Magnetism. Allen & Unwin: Springer, London. <http://dx.doi.org/10.1007/978-94-011-8036-8>

Wan, M., Schröder, C., & Peiffer, S. (2017). Fe(III):S(-II) Concentration Ratio Controls the Pathway and the Kinetics of Pyrite Formation during Sulfidation of Ferric Hydroxides, *Geochimica et Cosmochimica Acta*. doi: <http://dx.doi.org/10.1016/j.gca.2017.08.036>

Weber, M. E., Wiedicke, M. H., Kudrass, H. R., Hubscher, C. & Erlenkeuser, H. (1997). Active growth of the Bengal Fan during sea-level rise and highstand, *Geology*, 25(4), 315-318. [https://doi.org/10.1130/0091-7613\(1997\)025<0315:AGOTBF>2.3.CO;2](https://doi.org/10.1130/0091-7613(1997)025<0315:AGOTBF>2.3.CO;2)

Weber, M. E., Wiedicke-Hombach, M., Kudrass, H. R. & Erlenkeuser, H. (2003). Bengal Fan sediment transport activity and response to climate forcing inferred from sediment physical properties, *Sedimentary Geology*, 155(3-4), 361-381. [https://doi.org/10.1016/S0037-0738\(02\)00187-2](https://doi.org/10.1016/S0037-0738(02)00187-2)

Weber, M. E., & Reilly, B. T. (2018). Hemipelagic and turbiditic deposits constrain lower Bengal Fan depositional history through Pleistocene climate, monsoon, and sea level transitions. *Quaternary Science Reviews*, 199, 159-173. <https://doi.org/10.1016/j.quascirev.2018.09.027>

Werne, J.P., Lyons, T.W., Hollander, D.J., Schouten, S., Hopmans, E.C., & Damsté, J.S.S., (2008). Investigating pathways of diagenetic organic matter sulfurization using compound-specific sulfur isotope analysis. *Geochim. Cosmochim. Acta*, 72, 3489 – 3502. <https://doi.org/10.1016/j.gca.2008.04.033>

Wetzel, A., & Wijayananda, N. P. (1990). Biogenic sedimentary structures in outer Bengal Fan deposits drilled during Leg 116. In *Proceedings of the Ocean Drilling Project, Scientific Results* (No. 116, pp. 15-24). DOI: 10.2973/odp.proc.sr.116.114.1990.

Wing, B. A., & Halevy, I. (2014). Intracellular metabolite levels shape sulfur isotope fractionation during microbial sulfate respiration. *Proceedings of the National Academy of Sciences*, 111(51), 18116-18125.

Wortmann, U. G., Bernasconi, S. M. & Bottcher, M. E. (2001). Hypersulfidic deep biosphere indicates extreme sulfur isotope fractionation during single-step microbial sulfate reduction. *Geology*, 29(7), 647-650. [https://doi.org/10.1130/0091-7613\(2001\)029<0647:HDBIES>2.0.CO;2](https://doi.org/10.1130/0091-7613(2001)029<0647:HDBIES>2.0.CO;2)

Yucel, M., Konovalov, S. K., Moore, T. S., Janzen, C. P. & Luther III, G. W. (2010a). Sulfur speciation in the upper Black Sea sediments. *Chemical Geology*, 269(3-4), 364-375. <https://doi.org/10.1016/j.chemgeo.2009.10.010>

Yucel, M., Luther III, G. W. & Moore, W. S. (2010b). Earthquake-induced turbidite deposition as a previously unrecognized sink for hydrogen sulfide in the Black Sea sediments. *Marine Chemistry*, 121(1-4), 176-186. <https://doi.org/10.1016/j.marchem.2010.04.006>

Figure captions

Figure 1 Bathymetry map of Bay of Bengal showing the location of the cores MD161/29 (present study) and MD12-3417 (Fournier et al 2017); upper, middle and lower fan boundaries of Bengal fan and the presently active channel (Emmel and Curray, 1983). EEZ = exclusive economic zone.

Figure-2: Sub-bottom profiler image of the levee section showing hemipelagic (Hemi) and turbidite (Trb) depositional sequences (bracketed). Location of MD161/29 is marked by an arrow. The expanded SBP profile shows hemipelagic and (hemi) and turbidite (Trb) dominated sequences. The coring length below the sea bed is demarcated by a blue coloured dotted double-ended arrow. Vertical exaggeration = 3.6x

Figure-3: (A) Age-depth curve of the core MD161/29. The olive green and black colors of core log demarcate the hemipelagic (0-16 mbsf) and turbidite (16-30 mbsf) sedimentary sequences respectively. The turbidite layers are demarcated by light green bands. The blue and black dotted lines with double arrows indicate the vertical expanses of turbidite dominated and hemipelagic dominated sedimentary sequences; (B) D₅₀ grain size (μm) profile; (C) Wet bulk density (g/cm^3) profile; (D) Magnetic susceptibility (SI) profile; (E) Calcium carbonate (CaCO_3) content (wt%) profile and (F) total organic carbon content (wt%) profile. The D₅₀ and CaCO_3 contents in (B) and (E) for the turbidite zone are demarcated by red lines.

Figure-4. (A) Profiles of AVS content (wt%) and $\delta^{34}\text{S}_{\text{AVS}}$ (‰ VCDT) values; (B) profiles of CRS content (wt%) and $\delta^{34}\text{S}_{\text{CRS}}$ values; (C) profile of elemental sulfur content (wt%), (D) profile of total reducible sulfur content (TRIS) and (E) profiles of Fe_{ox} and Fe_{tr} contents (wt%).

Figure 5: Cross plot of $\delta^{34}\text{S}_{\text{CRS}}$ vs $\delta^{34}\text{S}_{\text{AVS}}$ values in core MD161-29.

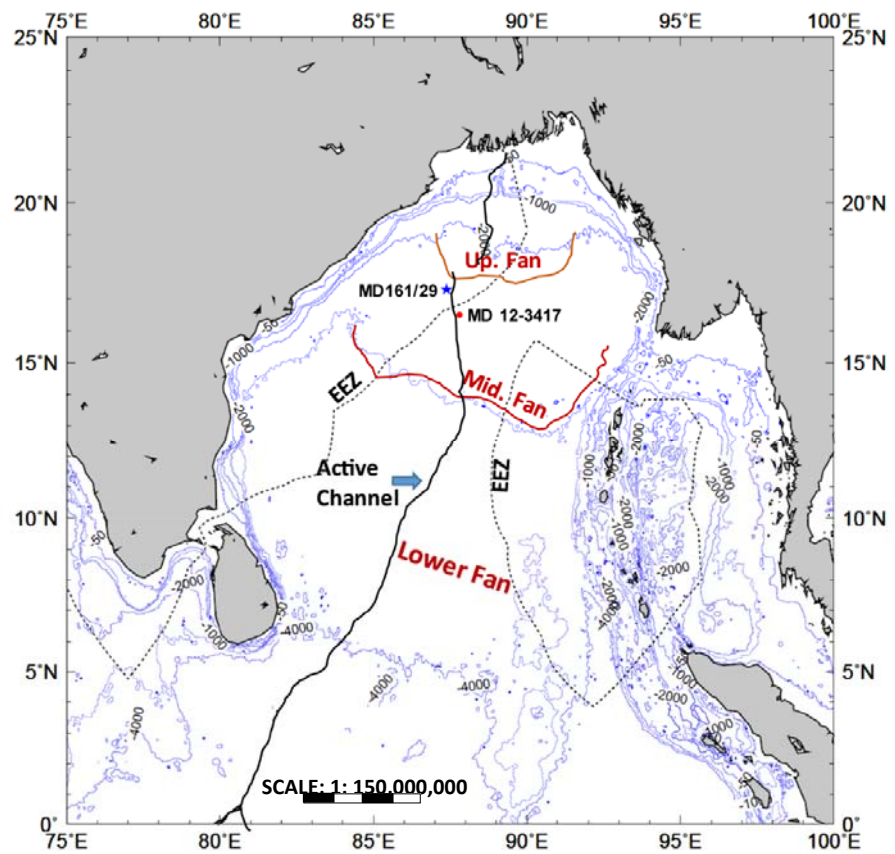


Figure 1

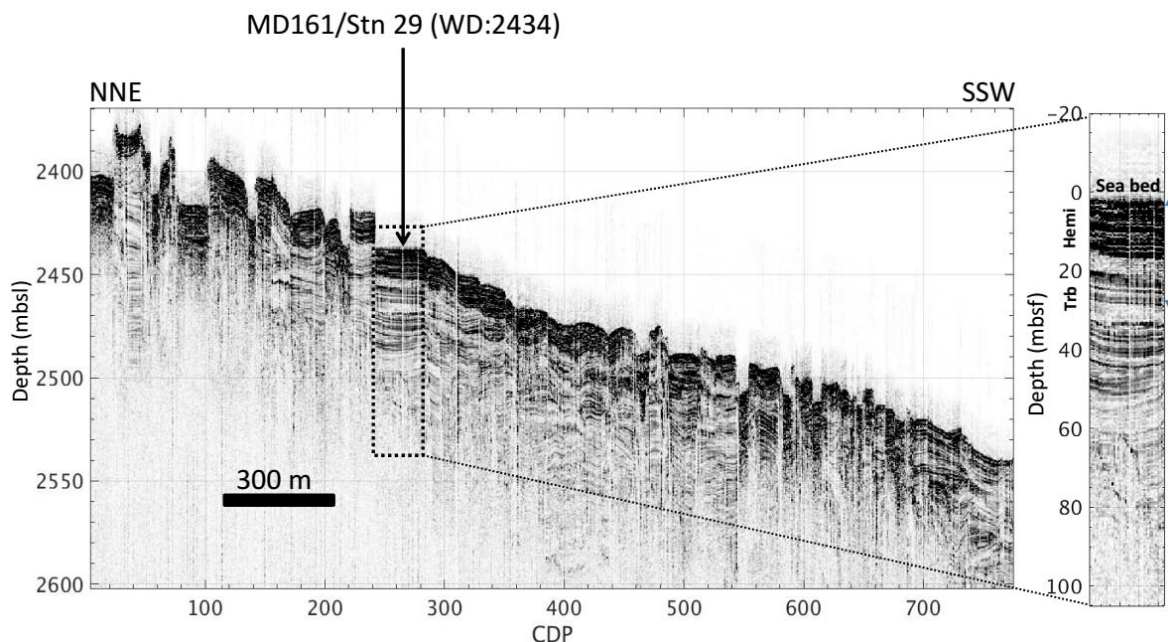


Figure 2

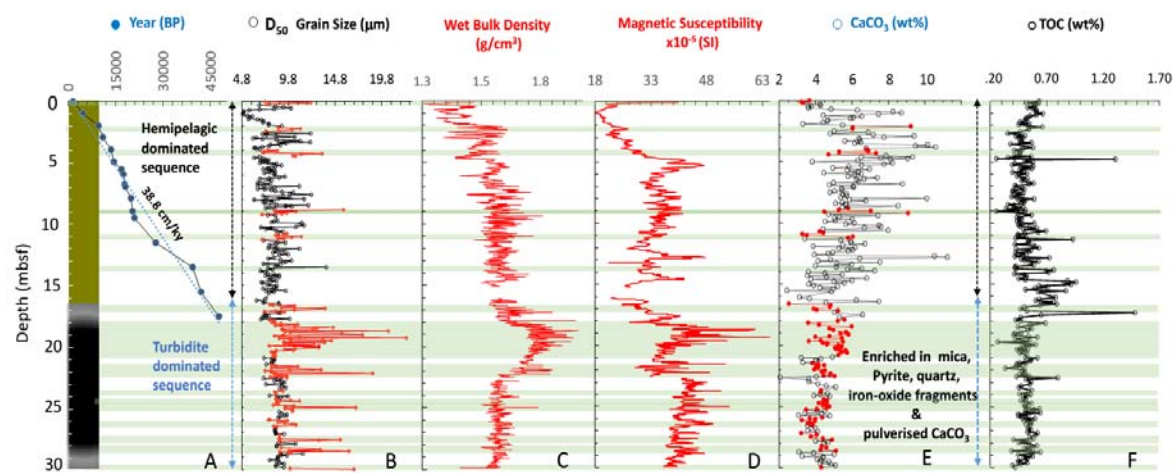


Figure 3

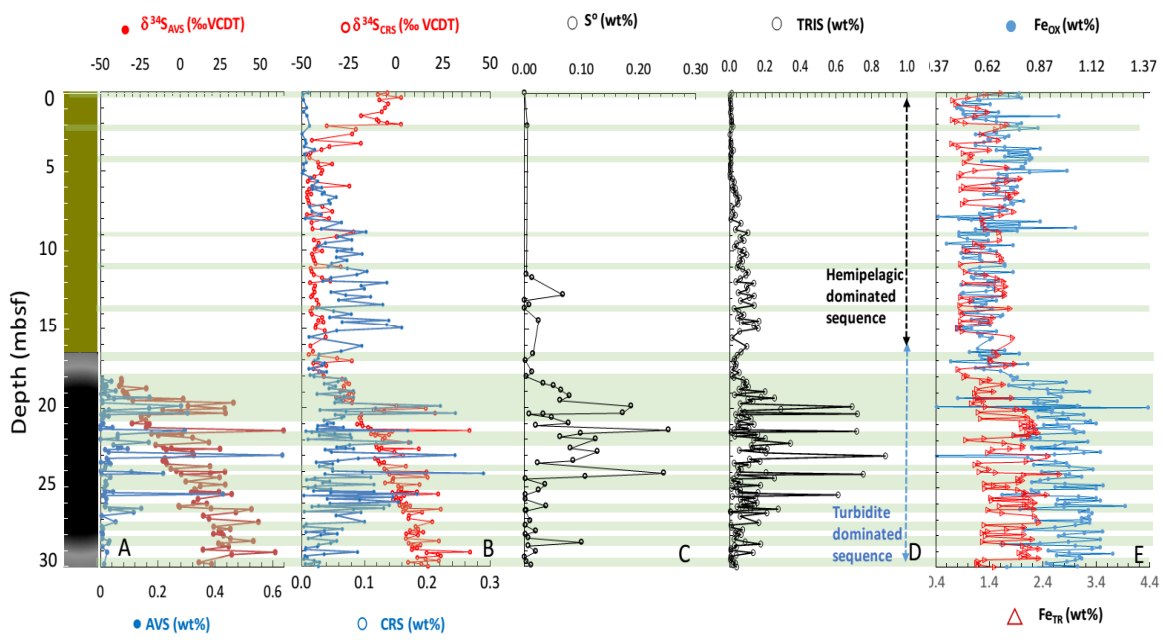


Figure 4

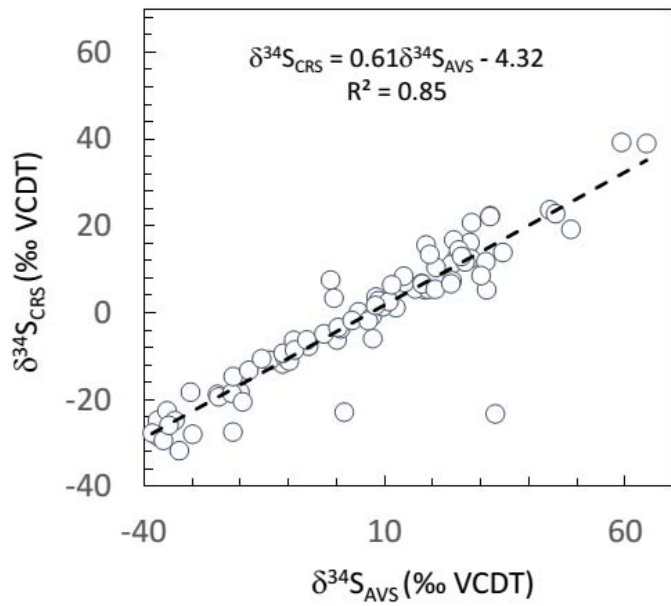


Figure 5

Supplementary Material

Contrasting sulfidization in the turbidite and hemipelagic sediments of Bengal Fan

S.Volvoikar¹, A. Mazumdar^{1*}, A. Peketi¹, P. Dewangan¹, B. Sawant¹, A. Manaskanya¹, H. Goswami², D. Das³, S. Pujari¹

¹Geological Oceanography, CSIR-National Institute of Oceanography, Dona Paula, Goa-403004, India

²School of Physical, Chemical & Applied SciencesDepartment of Earth Sciences Pondicherry University, Puducherry-605014, India

³Presidency University,86/1, College Street,Kolkata 700 073, India

*Correspondence: maninda@nio.org

Content : **Supplementary figure 1: Sedimentation rate profile Geological Map**

Supplementary Figure 2: Scatter plot of (TOC/TN)_{molar} vs □□¹³C_{TOC} Sub-bottom profiler data

Supplementary Figure -3: Supplementary Figure 3 : Histograms showing distribution of A:CRS (wt.%); B: $\delta^{34}\text{S}_{\text{CRS}}$ (‰ V-CDT); C:AVS (wt.%) and D: $\delta^{34}\text{S}_{\text{AVS}}$ (‰ V-CDT) . Red= Data points from Hemipelagic rich facies; Black= Data points from Turbidite rich facies.**Supplementary Table-1:Magnetic susceptibility (MS) and wet bulk density (WBD) data**

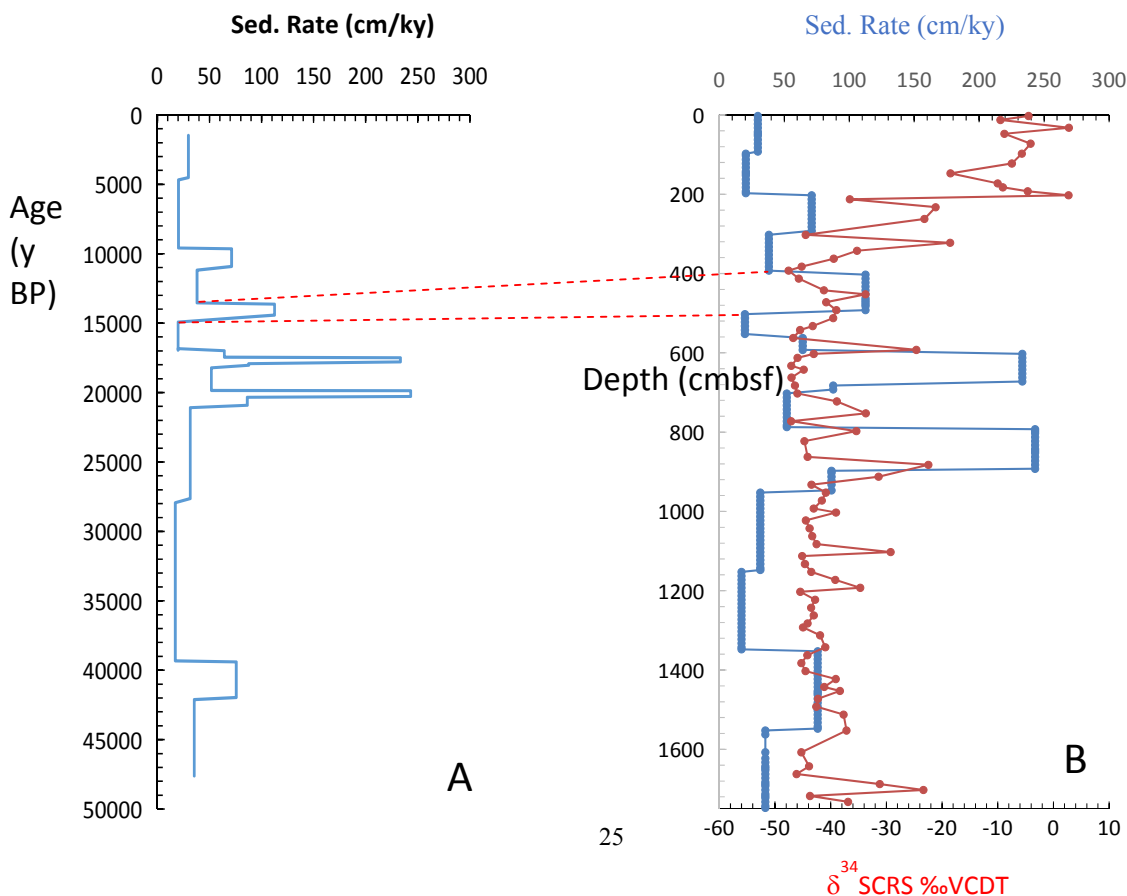
Supplementary Table-2:Radiocarbon Ages

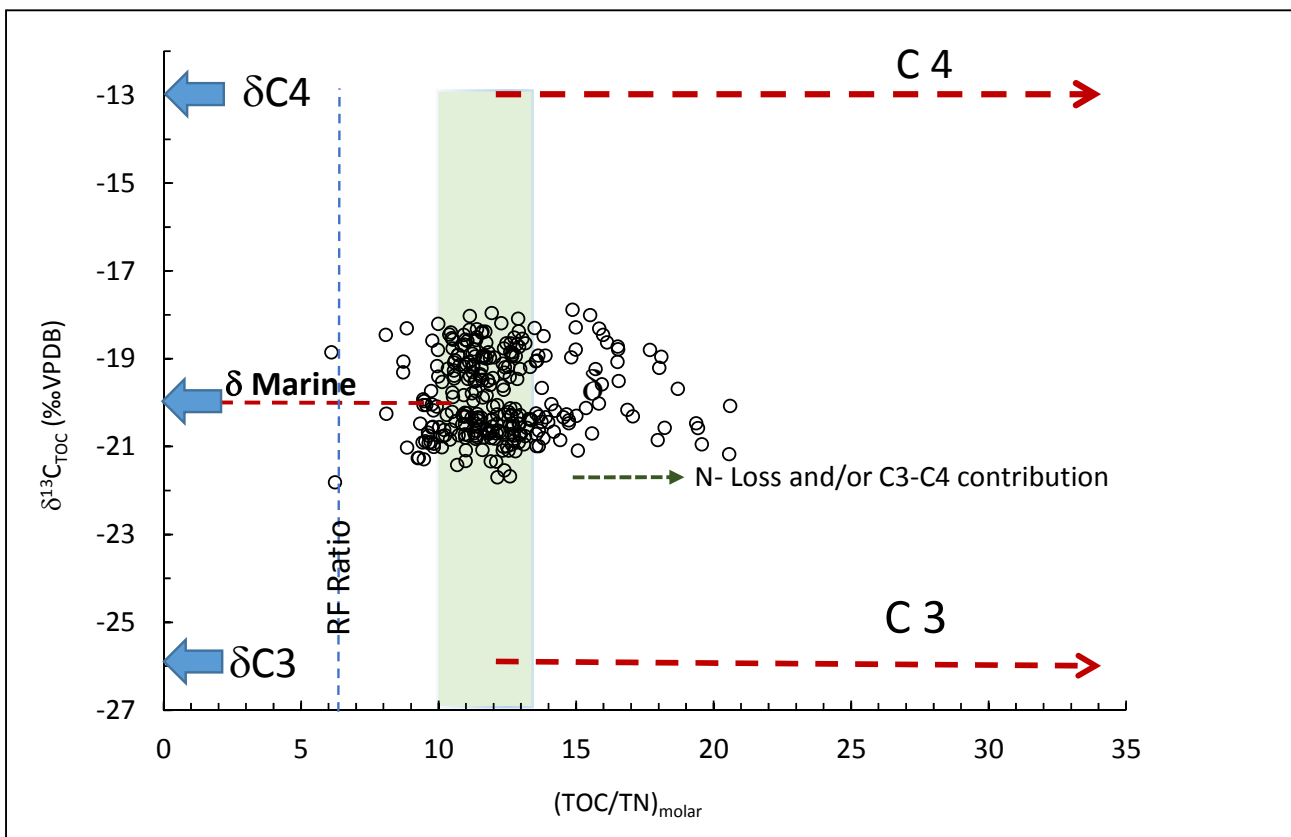
Supplementary Table-3: D₅₀ grain size data

Supplementary Table-4: CaCO₃ (wt%) TOC (wt%), TOC/TN and □¹³C_{TOC} data

Supplementary Table-5: Geochemical Data

Supplementary Figure-1: A. Temporal variation in sedimentation rate and (B) depthwise (cmbsf) variation in sedimentation rate and $\delta^{34}\text{S}_{\text{CRS}}$ profiles of the core MD161/29 (Hemipelagic dominated zone). The dotted line shows the zone of enhanced sedimentation rate and ³⁴S enrichment during the 14-15 ky (400-500 cmbsf) time span.

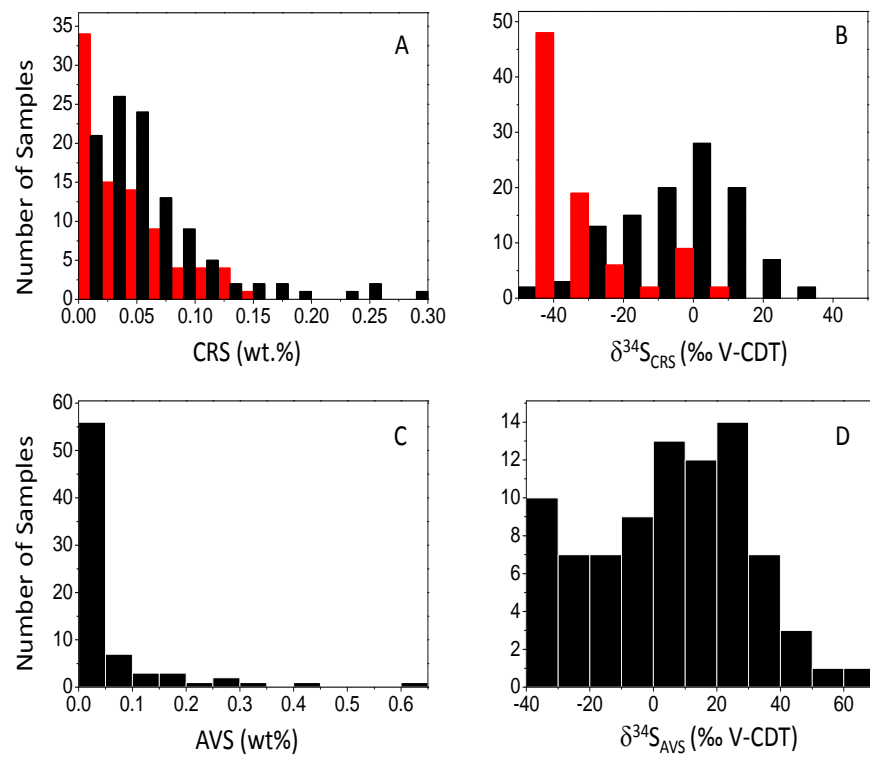




Supplementary Figure 2: Scatter plot of $(\text{TOC}/\text{TN})_{\text{molar}}$ vs $\delta^{13}\text{C}_{\text{TOC}}$ of sediment core MD161/29. The blue short arrows show approximate end member $\delta^{13}\text{C}$ values of terrestrial C3, C4 vegetation and marine phytoplankton (Tyson, 1995). Blue dotted line indicate $(\text{TOC}/\text{TN})_{\text{molar}}$ Redfield ratio (RF = Redfield Ratio). The light green shaded region is the approximate transition range of $(\text{TOC}/\text{TN})_{\text{molar}}$ between marine and terrestrial organic matter. The brown dotted arrows indicate increasing contribution of C3, C4 or marine organic matter the bulk organic matter.

Reference:

Tyson, R.V. (1995) Sedimentary Organic Matter, Organic facies and palynofacies. Chapman and Hall (London), p615



Supplementary Figure 3 : Histograms showing distribution of A:CRS (wt.%); B: $\delta^{34}\text{S}_{\text{CRS}}(\text{\textperthousand} \text{V-CDT})$; C:AVS (wt.%) and D: $\delta^{34}\text{S}_{\text{AVS}}(\text{\textperthousand} \text{V-CDT})$. Red= Data points from Hemipelagic rich facies; Black= Data points from Turbidite rich facies.

Supplementary Table-1 : Magnetic susceptibility (MS) and wet bulk density (WBD) data of the core MD161-29

Depth (cmbsf)	WBD (g/cm3)	MS 10 ⁻⁵ (SI)
0.10	1.47	40.3
0.12	1.35	32.3
0.14	1.37	28.6
0.16	1.37	26.4
0.18	1.36	24.8
0.20	1.35	23.6
0.22	1.24	22.5
0.24	1.29	21.6
0.26	1.28	21.4
0.28	1.29	21.1
0.30	1.28	21.4
0.32	1.32	22
0.34	1.35	22.7
0.36	1.37	23.4
0.38	1.41	24
0.40	1.45	24
0.42	1.46	23.8
0.44	1.48	23.5
0.46	1.44	22.9
0.48	1.44	22.5
0.50	1.41	22
0.52	1.47	21.4
0.54	1.47	21.1
0.56	1.42	20.8
0.58	1.41	20.7
0.60	1.43	20.9
0.62	1.41	20.9
0.64	1.4	20.7
0.66	1.34	20.5
0.68	1.3	20.1
0.70	1.37	20
0.72	1.4	19.8
0.74	1.38	19.8
0.76	1.38	19.7
0.78	1.36	19.4
0.80	1.36	18.9
0.82	1.34	18.7
0.84	1.34	18.5
0.86	1.32	18.4
0.88	1.33	18.3
0.90	1.33	18.3
0.92	1.33	18.3

0.94	1.34	18.4
0.96	1.35	18.4
0.98	1.35	18.5
1.00	1.37	18.6
1.02	1.35	18.7
1.04	1.38	19
1.06	1.4	19.2
1.08	1.4	19.4
1.10	1.43	19.5
1.12	1.42	19.5
1.14	1.42	19.5
1.16	1.41	19.4
1.18	1.46	19.5
1.20	1.45	19.5
1.22	1.45	19.5
1.24	1.44	19.4
1.26	1.42	19.6
1.28	1.44	20
1.30	1.42	20.6
1.32	1.44	20.7
1.34	1.44	20.8
1.36	1.41	20.7
1.38	1.31	20
1.40	1.32	19.7
1.42	1.32	19.8
1.44	1.36	20
1.59	1.35	20.6
1.61	1.34	20.2
1.63	1.34	20
1.65	1.37	20
1.67	1.37	20
1.69	1.37	20
1.71	1.35	20
1.73	1.36	20.1
1.75	1.37	20.2
1.77	1.39	20.7
1.79	1.39	21.1
1.81	1.39	21.4
1.83	1.45	21.6
1.85	1.38	21.6
1.87	1.43	21.9
1.89	1.4	22.2
1.91	1.48	22.3
1.93	1.46	22.3

1.95	1.47	22.4
1.97	1.48	22.5
1.99	1.51	22.4
2.01	1.52	22.4
2.03	1.52	22.3
2.05	1.54	22.3
2.07	1.56	22.9
2.09	1.59	23.5
2.11	1.44	23.9
2.13	1.44	24.5
2.15	1.4	24.8
2.17	1.53	25.1
2.19	1.57	25.3
2.21	1.49	25.4
2.23	1.51	25.9
2.25	1.57	26.4
2.27	1.55	26.7
2.29	1.61	26.9
2.31	1.6	26.7
2.33	1.61	25.9
2.35	1.51	24.6
2.37	1.5	23.7
2.39	1.49	22.8
2.41	1.48	22.7
2.43	1.48	22.8
2.45	1.48	23.1
2.47	1.42	23.1
2.49	1.37	22.7
2.51	1.36	22.4
2.53	1.39	22.1
2.55	1.46	21.9
2.57	1.5	21.9
2.59	1.51	22.2
2.61	1.53	22.6
2.63	1.57	23.4
2.65	1.6	24.1
2.67	1.56	24.6
2.69	1.51	24.1
2.71	1.5	23.1
2.73	1.46	21.9
2.75	1.39	21
2.77	1.45	20.9
2.79	1.55	21.5
2.81	1.57	22.1

2.83	1.57	22.4
2.85	1.52	22.7
2.87	1.53	23.1
2.89	1.59	23.6
2.91	1.53	23.9
2.93	1.51	23.8
2.95	1.37	23.3
2.97	1.34	22.7
3.07	1.49	24.9
3.09	1.48	24.9
3.11	1.48	24.9
3.13	1.51	25
3.15	1.5	25.1
3.17	1.51	25.9
3.19	1.51	26.4
3.21	1.52	27.1
3.23	1.53	27.6
3.25	1.54	28.1
3.27	1.55	27.9
3.29	1.51	27.3
3.31	1.5	26.5
3.33	1.48	26.1
3.35	1.5	25.8
3.37	1.52	25.8
3.39	1.51	25.8
3.41	1.5	26
3.43	1.51	26.4
3.45	1.57	26.9
3.47	1.53	27.1
3.49	1.5	26.7
3.51	1.47	26.2
3.53	1.47	25.8
3.55	1.48	26
3.57	1.48	26.2
3.59	1.51	26.8
3.61	1.55	27.5
3.63	1.49	28
3.65	1.5	27.7
3.67	1.47	27.2
3.69	1.46	26.8
3.71	1.48	26.8
3.73	1.47	26.8
3.75	1.47	26.4
3.77	1.47	26.4

3.79	1.46	26.2
3.81	1.46	25.9
3.83	1.46	25.8
3.85	1.44	24.9
3.87	1.45	25.8
3.89	1.46	26.1
3.91	1.45	26.5
3.93	1.47	26.8
3.95	1.48	27.2
3.97	1.48	27.3
3.99	1.49	27.4
4.01	1.49	27.8
4.03	1.49	28.1
4.05	1.49	28.9
4.07	1.51	30
4.09	1.52	30.5
4.11	1.57	30.4
4.13	1.5	30
4.15	1.47	29.2
4.17	1.45	28.7
4.19	1.48	28.4
4.21	1.45	28.1
4.23	1.45	28
4.25	1.47	28.2
4.27	1.52	28.9
4.29	1.51	29.9
4.31	1.58	30.8
4.33	1.5	31.3
4.35	1.5	31.4
4.37	1.47	31
4.39	1.46	30.6
4.41	1.43	30.7
4.43	1.47	31.3
4.45	1.5	31.8
4.57	1.39	31.2
4.59	1.39	31.9
4.61	1.4	32.9
4.63	1.46	33.8
4.65	1.42	34.2
4.67	1.39	34.5
4.69	1.42	34.8
4.71	1.47	35.3
4.73	1.52	35.9
4.75	1.53	37

4.77	1.55	38.4
4.79	1.56	40
4.81	1.56	41.3
4.83	1.55	42
4.85	1.55	42.3
4.87	1.54	42.1
4.89	1.55	41.6
4.91	1.52	41.1
4.93	1.53	41
4.95	1.52	40.7
4.97	1.52	40.4
4.99	1.53	39.5
5.01	1.53	38.4
5.03	1.53	37.7
5.05	1.53	37.3
5.07	1.58	38.1
5.09	1.59	39.6
5.11	1.6	41.9
5.13	1.58	44.5
5.15	1.57	46
5.17	1.57	46.5
5.19	1.56	46.3
5.21	1.59	46.3
5.23	1.59	46.8
5.25	1.58	47.3
5.27	1.59	47.3
5.29	1.6	46.6
5.31	1.57	45.8
5.33	1.58	45
5.35	1.61	45
5.37	1.61	45.2
5.39	1.62	44.9
5.41	1.57	43.7
5.43	1.54	41.7
5.45	1.53	39
5.47	1.52	37.1
5.49	1.54	36.1
5.51	1.54	35.7
5.53	1.55	36.3
5.55	1.58	36.9
5.57	1.58	37.8
5.59	1.58	38.7
5.61	1.57	39.8
5.63	1.56	40.6

5.65	1.54	40.6
5.67	1.55	40.4
5.69	1.55	39.8
5.71	1.56	39.1
5.73	1.56	38.6
5.75	1.58	38.6
5.77	1.56	38.9
5.79	1.55	38.7
5.81	1.54	38.3
5.83	1.55	37.6
5.85	1.53	36.5
5.87	1.52	35
5.89	1.51	33.7
5.91	1.53	33
5.93	1.57	33.5
6.06	1.43	36.4
6.08	1.41	36.1
6.10	1.42	35.8
6.12	1.48	35.8
6.14	1.51	36.1
6.16	1.53	36.5
6.18	1.51	36.6
6.20	1.51	35.8
6.22	1.53	35.1
6.24	1.51	34.1
6.26	1.51	33.3
6.28	1.5	32.9
6.30	1.51	32.8
6.32	1.51	32.8
6.34	1.53	32.7
6.36	1.52	32.7
6.38	1.54	32.6
6.40	1.56	32.7
6.42	1.55	33
6.44	1.57	33.2
6.46	1.57	33.8
6.48	1.59	34.2
6.50	1.59	34.8
6.52	1.59	35.1
6.54	1.53	34.4
6.56	1.51	33.2
6.58	1.51	32.1
6.60	1.5	31.2
6.62	1.49	30.5

6.64	1.5	30.2
6.66	1.54	30
6.68	1.54	30.1
6.70	1.54	30.4
6.72	1.56	31
6.74	1.6	31.7
6.76	1.56	32.7
6.78	1.54	33.2
6.80	1.51	33.3
6.82	1.51	33
6.84	1.51	32.5
6.86	1.52	31.9
6.88	1.52	31.7
6.90	1.56	32.1
6.92	1.58	33.5
6.94	1.6	35.1
6.96	1.66	36.3
6.98	1.6	36.3
7.00	1.53	35.3
7.02	1.52	34.1
7.04	1.52	32.8
7.06	1.52	31.8
7.08	1.52	31.4
7.10	1.53	31.5
7.12	1.56	32.1
7.14	1.57	31.8
7.16	1.57	31.8
7.18	1.57	32.3
7.20	1.64	33
7.22	1.65	33.9
7.24	1.61	35
7.26	1.59	37.2
7.28	1.66	36.1
7.30	1.64	35.1
7.32	1.61	35.3
7.34	1.64	35.4
7.36	1.62	35.2
7.38	1.64	35.1
7.40	1.63	35.5
7.42	1.61	38.3
7.44	1.71	39.8
7.58	1.48	35.3
7.60	1.44	35.1
7.62	1.45	34.7

7.64	1.56	35.2
7.66	1.51	35.8
7.68	1.44	34.8
7.70	1.48	33.1
7.72	1.55	32.6
7.74	1.56	32.9
7.76	1.61	34.2
7.78	1.65	36.6
7.80	1.58	39.5
7.82	1.59	41.1
7.84	1.54	40.2
7.86	1.54	38
7.88	1.57	36.8
7.90	1.61	37
7.92	1.63	37.7
7.94	1.58	38
7.96	1.61	39.1
7.98	1.68	40.4
8.00	1.58	40.9
8.02	1.54	40.2
8.04	1.53	38.9
8.06	1.53	37.8
8.08	1.54	36.9
8.10	1.56	36.5
8.12	1.56	36.4
8.14	1.54	36.7
8.16	1.53	36.6
8.18	1.53	36
8.20	1.53	35.3
8.22	1.52	34.6
8.24	1.48	34.7
8.26	1.5	34.8
8.28	1.54	33.7
8.30	1.52	32.7
8.32	1.5	31.7
8.34	1.5	31
8.36	1.55	31.3
8.38	1.61	32.7
8.40	1.6	34.3
8.42	1.57	35.5
8.44	1.59	36.7
8.46	1.57	37.3
8.48	1.62	37.6
8.50	1.67	37.7

8.52	1.56	36.5
8.54	1.54	35
8.56	1.57	34.6
8.58	1.62	35.7
8.60	1.58	36.9
8.62	1.54	37.2
8.64	1.52	37.1
8.66	1.55	38
8.68	1.59	39.7
8.70	1.57	41.2
8.72	1.58	41.2
8.74	1.53	39.2
8.76	1.52	36
8.78	1.51	33.2
8.80	1.55	32
8.82	1.59	32.8
8.84	1.66	35.2
8.86	1.6	38.3
8.88	1.59	40.7
8.90	1.59	41.1
8.92	1.62	40.2
8.94	1.59	38.3
8.96	1.57	36.9
9.07	1.54	35.8
9.09	1.6	35
9.11	1.68	35.1
9.13	1.59	35.1
9.15	1.58	35.3
9.17	1.62	36.7
9.19	1.54	39.3
9.21	1.54	41.3
9.23	1.55	41.6
9.25	1.55	40.2
9.27	1.55	38.2
9.29	1.57	36.5
9.31	1.55	35.1
9.33	1.58	34.8
9.35	1.61	36.1
9.37	1.76	38.1
9.39	1.54	37.4
9.41	1.51	35.2
9.43	1.52	33.4
9.45	1.53	32.7
9.47	1.55	32.7

9.49	1.57	34.1
9.51	1.69	36.3
9.53	1.7	36.7
9.55	1.53	34.7
9.57	1.56	33.4
9.59	1.62	33.4
9.61	1.64	34.3
9.63	1.65	35.5
9.65	1.72	36.9
9.67	1.6	37.2
9.69	1.6	36.8
9.71	1.62	36.9
9.73	1.6	36.8
9.75	1.53	35.1
9.77	1.53	34
9.79	1.56	33.9
9.81	1.58	34.7
9.83	1.64	35.6
9.85	1.63	35.8
9.87	1.52	35.2
9.89	1.5	34.6
9.91	1.55	35
9.93	1.61	36.1
9.95	1.64	36.9
9.97	1.55	36.4
9.99	1.53	34.6
10.00	1.54	33.1
10.00	1.58	32.7
10.00	1.67	32.9
10.10	1.62	33.2
10.10	1.59	33.5
10.10	1.64	33.7
10.10	1.6	34
10.10	1.55	33.9
10.20	1.59	33.8
10.20	1.65	34.2
10.20	1.61	35.6
10.20	1.55	36.4
10.20	1.59	37.1
10.30	1.54	38.2
10.30	1.51	39.3
10.30	1.56	39.6
10.30	1.58	39.3
10.30	1.58	38.3

10.40	1.61	37.3
10.40	1.55	36.9
10.40	1.54	36.3
10.40	1.53	35.2
10.40	1.54	33.9
10.60	1.53	32.9
10.60	1.5	34.5
10.60	1.53	34.7
10.60	1.52	34.4
10.70	1.61	33.9
10.70	1.61	33.4
10.70	1.59	32.4
10.70	1.54	31
10.70	1.54	29.8
10.80	1.6	29.8
10.80	1.63	30.3
10.80	1.65	31
10.80	1.51	31.3
10.80	1.51	31.9
10.90	1.52	33.4
10.90	1.6	35.9
10.90	1.63	37.2
10.90	1.59	35.8
10.90	1.61	34.6
11.00	1.64	34
11.00	1.54	33.4
11.00	1.59	33.9
11.00	1.62	35.4
11.00	1.72	36.1
11.10	1.52	35.3
11.10	1.53	34.6
11.10	1.6	35.2
11.10	1.64	35.5
11.10	1.57	33.2
11.20	1.53	31.9
11.20	1.56	31.3
11.20	1.54	31.2
11.20	1.61	31.6
11.20	1.61	32
11.30	1.58	32.3
11.30	1.47	32.4
11.30	1.48	32
11.30	1.52	31.7
11.30	1.48	31.6

11.40	1.56	31.6
11.40	1.55	31.8
11.40	1.62	31.7
11.40	1.58	31.3
11.40	1.62	31
11.50	1.63	30.1
11.50	1.54	29.4
11.50	1.54	29.2
11.50	1.56	29.4
11.50	1.57	29.9
11.60	1.56	30.3
11.60	1.56	30.3
11.60	1.57	30.3
11.60	1.55	31.2
11.60	1.55	31.7
11.70	1.57	32.1
11.70	1.57	32.5
11.70	1.58	32.6
11.70	1.55	32.4
11.70	1.54	32
11.80	1.56	31.9
11.80	1.51	32.3
11.80	1.53	32.4
11.80	1.54	32.3
11.80	1.59	32.1
11.90	1.53	31.9
11.90	1.52	31.5
11.90	1.52	30.6
11.90	1.56	29.7
11.90	1.57	28.7
12.00	1.63	28.2
12.10	1.56	26.6
12.10	1.61	27.6
12.10	1.58	28.5
12.10	1.57	29.4
12.20	1.63	30.5
12.20	1.65	31.4
12.20	1.64	32
12.20	1.66	32.6
12.20	1.61	32.8
12.30	1.53	32.5
12.30	1.53	31.8
12.30	1.59	31.9
12.30	1.64	32.6

12.30	1.65	33.3
12.40	1.57	33.7
12.40	1.57	34.1
12.40	1.59	34.6
12.40	1.58	35.1
12.40	1.61	35.5
12.50	1.6	35.8
12.50	1.55	36.3
12.50	1.6	36.9
12.50	1.62	37.6
12.50	1.61	37.6
12.60	1.61	37.4
12.60	1.61	37.1
12.60	1.59	36.7
12.60	1.59	36.4
12.60	1.57	35.9
12.70	1.59	36.1
12.70	1.58	37.6
12.70	1.55	39.8
12.70	1.59	42.6
12.70	1.61	45.9
12.80	1.58	47.6
12.80	1.58	46.4
12.80	1.6	43.3
12.80	1.57	41.6
12.80	1.56	42.6
12.90	1.53	43.9
12.90	1.58	41.8
12.90	1.59	37.4
12.90	1.58	34.1
12.90	1.58	32.5
13.00	1.55	32.4
13.00	1.52	32.4
13.00	1.59	32
13.00	1.59	31.7
13.00	1.56	31.9
13.10	1.53	32.3
13.10	1.54	32.5
13.10	1.61	32.1
13.10	1.61	31.4
13.10	1.61	31.3
13.20	1.57	31.7
13.20	1.62	31.9
13.20	1.62	32

13.20	1.6	21.6
13.20	1.51	33.3
13.30	1.52	33.9
13.30	1.56	34.1
13.30	1.56	34
13.30	1.6	33.5
13.30	1.6	33.2
13.40	1.56	32.7
13.40	1.54	32.3
13.40	1.55	31.7
13.40	1.54	31.1
13.40	1.57	30.8
13.50	1.59	30.8
13.60	1.62	35.6
13.60	1.61	35.3
13.60	1.54	34.3
13.60	1.58	33.5
13.70	1.57	32.9
13.70	1.6	32.7
13.70	1.6	32.6
13.70	1.58	32.4
13.70	1.61	32.3
13.80	1.65	32
13.80	1.62	31.5
13.80	1.56	30.4
13.80	1.51	29.8
13.80	1.52	29.4
13.90	1.53	29.7
13.90	1.57	29.9
13.90	1.55	30
13.90	1.54	30.1
13.90	1.56	30.4
14.00	1.59	30.5
14.00	1.55	30.5
14.00	1.55	30.2
14.00	1.53	30
14.00	1.58	30.2
14.10	1.57	30.6
14.10	1.63	31.6
14.10	1.64	32.8
14.10	1.7	33.7
14.10	1.59	33.7
14.20	1.59	33.5
14.20	1.62	33.9

14.20	1.63	34.6
14.20	1.64	35.3
14.20	1.6	35.7
14.30	1.56	35.5
14.30	1.6	34.8
14.30	1.59	34.6
14.30	1.66	35.1
14.30	1.69	35.4
14.40	1.64	35.4
14.40	1.63	35.5
14.40	1.65	36.1
14.40	1.65	37.1
14.40	1.6	37.7
14.50	1.61	37.6
14.50	1.63	37.7
14.50	1.65	
14.50	1.65	39.8
14.50	1.61	41.8
14.60	1.59	41.9
14.60	1.6	40
14.60	1.66	38.1
14.60	1.66	36.4
14.60	1.58	34.7
14.70	1.57	33.1
14.70	1.6	31.9
14.70	1.55	31.4
14.70	1.53	30.8
14.70	1.52	30.3
14.80	1.51	29.9
14.80	1.52	29.9
14.80	1.52	30
14.80	1.5	30.2
14.80	1.53	30
14.90	1.53	29.4
14.90	1.55	29.1
14.90	1.56	28.9
14.90	1.55	28.6
14.90	1.53	28.2
15.10	1.58	26.5
15.10	1.54	26.2
15.10	1.58	26
15.10	1.58	26.4
15.10	1.58	26.5
15.20		26.5

15.20		26.3
15.20		26.5
15.20		27.2
15.20		27.5
15.30		
15.30		
15.30		
15.30		
15.30		
15.40		
15.40		
15.40		
15.40		
15.40		
15.50		
15.50		
15.50		
15.50		
15.50		
15.60		
15.60		
15.60		
15.60		
15.60		
15.70		
15.70		
15.70		
15.70		
15.70		
15.70		
15.80		
15.80		
15.80		
15.80		
15.80		
15.90		
15.90		
15.90		
15.90		
15.90		
16.00		
16.00		
16.00		
16.00		
16.00		

16.10		
16.10		
16.10		
16.10	1.57	22.3
16.10	1.59	22.6
16.20	1.57	24.1
16.20	1.54	26.1
16.20	1.54	26.9
16.20	1.56	27.4
16.20	1.6	28.7
16.30	1.65	29.4
16.30	1.65	30.1
16.30	1.6	30.3
16.30	1.55	30.5
16.30	1.56	31
16.40	1.59	31.3
16.40	1.58	31.7
16.40	1.65	31.9
16.40	1.58	32.3
16.40	1.54	32.3
16.60	1.54	30.2
16.60	1.53	28.2
16.60	1.56	25.5
16.70	1.55	25.1
16.70	1.57	27.8
16.70	1.59	29.7
16.70	1.61	29.7
16.70	1.61	29
16.80	1.61	28.7
16.80	1.62	28.6
16.80	1.63	28.7
16.80	1.67	29.3
16.80	1.69	30
16.90	1.58	30.3
16.90	1.57	29.5
16.90	1.58	28.9
16.90	1.56	28.8
16.90	1.56	28.9
17.00	1.58	29
17.00	1.59	29.4
17.00	1.64	30.2
17.00	1.72	31.3
17.00	1.68	31.9
17.10	1.6	32

17.10	1.61	32
17.10	1.64	32.7
17.10	1.69	32.8
17.10	1.65	32.3
17.20	1.61	31.9
17.20	1.66	33.4
17.20	1.8	33
17.20	1.57	32.9
17.20	1.61	32.4
17.30	1.68	31.7
17.30	1.72	31.5
17.30	1.57	31.4
17.30	1.61	31.5
17.30	1.67	31.8
17.40	1.61	32
17.40	1.62	32.9
17.40	1.63	34.5
17.40	1.66	36.5
17.40	1.63	37.4
17.50	1.67	37.6
17.50	1.65	37.3
17.50	1.57	37.4
17.50	1.58	38.1
17.50	1.58	38.7
17.60	1.56	39.4
17.60	1.6	40.3
17.60	1.6	40.5
17.60	1.61	40.8
17.60	1.62	40.5
17.70	1.61	39.9
17.70	1.62	38.5
17.70	1.61	36.4
17.70	1.61	35
17.70	1.62	35.5
17.80	1.62	37.3
17.80	1.61	38.5
17.80	1.57	
17.80	1.59	37.7
17.80	1.62	36.3
17.90	1.58	34.3
17.90	1.65	32.8
17.90	1.7	33
17.90	1.9	34.6
17.90	1.62	35.8

18.00	1.62	35
18.00	1.61	33.9
18.00	1.65	33.3
18.10	1.63	27.3
18.10	1.66	28.2
18.10	1.6	28.9
18.10	1.7	30
18.10	1.7	32.1
18.20	1.72	35.3
18.20	1.77	37.7
18.20	1.62	35.9
18.20	1.68	34.1
18.20	1.69	34.2
18.30	1.63	34.4
18.30	1.65	36
18.30	1.68	39.3
18.30	1.75	42.5
18.30	1.68	42.1
18.40	1.72	41
18.40	1.73	40.8
18.40	1.68	41.8
18.40	1.8	45
18.40	1.73	45.3
18.50	1.71	44.5
18.50	1.76	47.2
18.50	1.77	48.3
18.50	1.74	45.5
18.50	1.73	43.9
18.60	1.8	42.9
18.60	1.69	40.9
18.60	1.71	40.3
18.60	1.73	40.6
18.60	1.72	39.4
18.70	1.7	38.7
18.70	1.75	41.7
18.70	1.79	47.6
18.70	1.91	55.4
18.70	1.9	61
18.80	1.84	58.7
18.80	1.75	49.9
18.80	1.71	43.9
18.80	1.77	43.3
18.80	1.83	45
18.90	1.71	43.9

18.90	1.71	42.3
18.90	1.75	44.3
18.90	1.81	46.2
18.90	1.71	43.6
19.00	1.7	41.3
19.00	1.74	42
19.00	1.76	44
19.00	1.86	45.9
19.00	1.75	44.7
19.10	1.7	42.4
19.10	1.78	45.6
19.10	1.86	50.9
19.10	1.78	51.4
19.10	1.73	44.9
19.20	1.75	40.4
19.20	1.7	38.4
19.20	1.75	39.9
19.20	1.78	43.6
19.20	1.84	48.9
19.30	1.89	56.9
19.30	1.87	64.9
19.30	1.85	62.6
19.30	1.69	50
19.30	1.78	42.9
19.40	1.73	41
19.40	1.75	41.3
19.40	1.78	42.9
19.40	1.71	40.8
19.40	1.73	38.3
19.60	1.74	40.8
19.60	1.8	45.2
19.60	1.88	53.4
19.60	1.72	48.9
19.70	1.73	42
19.70	1.78	41.7
19.70	1.81	44.8
19.70	1.72	42.4
19.70	1.74	39.8
19.80	1.78	40.7
19.80	1.73	39
19.80	1.73	36.4
19.80	1.72	36.7
19.80	1.76	39.5
19.90	1.81	44

19.90	1.84	47.6
19.90	1.77	43.5
19.90	1.71	37.2
19.90	1.71	34.2
20.00	1.73	35
20.00	1.75	38.9
20.00	1.79	43.7
20.00	1.75	43.5
20.00	1.77	38.9
20.10	1.74	36.9
20.10	1.76	37.8
20.10	1.74	38
20.10	1.7	35.7
20.10	1.71	35.3
20.20	1.72	36.5
20.20	1.75	38.1
20.20	1.78	39.5
20.20	1.7	39.1
20.20	1.78	38.1
20.30	1.71	37.1
20.30	1.74	37.8
20.30	1.75	39.4
20.30	1.79	39.3
20.30	1.72	37.1
20.40	1.73	35.7
20.40	1.73	35.1
20.40	1.73	34.7
20.40	1.7	34.7
20.40	1.74	35.6
20.50	1.74	37.1
20.50	1.72	38.2
20.50	1.74	39.1
20.50	1.76	39.4
20.50	1.72	37.4
20.60	1.73	35.5
20.60	1.73	35.1
20.60	1.74	35.2
20.60	1.73	36.4
20.60	1.71	36.7
20.70	1.72	36.7
20.70	1.72	37.4
20.70	1.72	38.6
20.70	1.72	38.7
20.70	1.69	37.2

20.80	1.71	35.4
20.80	1.68	34.4
20.80	1.72	34.1
20.80	1.71	34.5
20.80	1.72	35.1
20.90	1.69	35.2
20.90	1.69	35.1
20.90	1.69	34.5
20.90	1.68	34.3
20.90	1.69	35.2
21.00	1.71	36.7
21.10	1.72	34.5
21.10	1.7	33.5
21.10	1.69	33.8
21.10	1.71	33.7
21.20	1.69	33.5
21.20	1.67	33.7
21.20	1.68	33.5
21.20	1.68	33.8
21.20	1.66	33.8
21.30	1.68	33.5
21.30	1.67	35.1
21.30	1.7	38.4
21.30	1.67	40.3
21.30	1.68	39.6
21.40	1.67	43
21.40	1.68	37.9
21.40	1.67	35.9
21.40	1.69	37
21.40	1.69	38.9
21.50	1.7	42
21.50	1.75	48.2
21.50	1.76	52.9
21.50	1.69	47.2
21.50	1.69	37.6
21.70	1.72	40.6
21.70	1.71	40.2
21.70	1.74	35.5
21.70	1.76	31.9

21.70	1.66	30.3
21.80	1.68	29.2
21.80	1.63	28.7
21.80	1.65	28.9
21.80	1.64	30.2
21.80	1.67	32.8
21.90	1.68	36.7
21.90	1.67	40.7
21.90	1.7	43
21.90	1.73	40.7
21.90	1.8	37.1
22.00	1.73	36
22.00	1.72	34
22.00	1.79	32.4
22.00	1.62	32
22.00	1.67	31.4
22.10	1.68	31.7
22.10	1.64	
22.10	1.69	33.4
22.10	1.68	35.4
22.10	1.68	38.2
22.20	1.69	42.6
22.20	1.72	48.7
22.20	1.75	48.7
22.20	1.79	41
22.20	1.67	35.8
22.30	1.66	33.8
22.30	1.64	33.3
22.30	1.58	33.8
22.30	1.6	34.7
22.30	1.57	35.4
22.40	1.6	35.1
22.40	1.59	34.6
22.40	1.59	34.8
22.40	1.62	35.3
22.40	1.58	34.2
22.50	1.6	33.1
22.50	1.64	32.8
22.70	1.57	42.2
22.70	1.58	42.5

22.70	1.59	42.2
22.70	1.58	41.9
22.70	1.58	41.3
22.80	1.56	41.4
22.80	1.62	43.2
22.80	1.66	44.3
22.80	1.6	43.1
22.80	1.56	42.3
22.90	1.56	42.3
22.90	1.58	42.7
22.90	1.58	43.3
22.90	1.59	44.5
22.90	1.59	44.4
23.00	1.58	44.2
23.00	1.54	44.7
23.00	1.56	46.9
23.00	1.57	48.1
23.00	1.57	47.6
23.10	1.57	45.8
23.10	1.59	43.6
23.10	1.56	42.1
23.10	1.54	41.5
23.10	1.54	41.9
23.20	1.57	44.1
23.20	1.61	46.7
23.20	1.57	47
23.20	1.58	46.2
23.20	1.57	44.4
23.30	1.56	42.9
23.30	1.56	42.6
23.30	1.57	43.6
23.30	1.58	45.2
23.30	1.55	45.2
23.40	1.56	44.3
23.40	1.56	44.2
23.40	1.59	44.6
23.40	1.61	44.4
23.40	1.58	42.8
23.50	1.57	42.2
23.50	1.57	42.3
23.50	1.57	43.4
23.50	1.57	44
23.50	1.57	43.8
23.60	1.58	44

23.60	1.59	44.4
23.60	1.6	44.7
23.60	1.55	43.6
23.60	1.57	43
23.70	1.57	44.1
23.70	1.58	45.9
23.70	1.61	49.7
23.70	1.58	51.8
23.70	1.56	47.6
23.80	1.55	43.2
23.80	1.57	41.8
23.80	1.56	41.5
23.80	1.54	41.8
23.80	1.57	42.7
23.90	1.59	42.8
23.90	1.56	42.3
23.90	1.56	41.9
23.90	1.54	41.3
23.90	1.58	41.3
24.00	1.59	41.9
24.00	1.61	42.3
24.00	1.63	43
24.10	1.58	42
24.10	1.59	42.5
24.10	1.6	43.5
24.10	1.66	45.1
24.20	1.54	44.3
24.20	1.55	41.7
24.20	1.56	39.9
24.20	1.53	39.3
24.20	1.58	38.9
24.30	1.56	39.4
24.30	1.54	40.1
24.30	1.56	40.3
24.30	1.55	40.4
24.30	1.57	41
24.40	1.58	42.5
24.40	1.57	43.8
24.40	1.59	45.4
24.40	1.58	46.4
24.40	1.57	47
24.50	1.59	47.3
24.50	1.59	45.9
24.50	1.56	43.5

24.50	1.54	42
24.50	1.54	41.5
24.60	1.58	41.7
24.60	1.57	41.7
24.60	1.55	41
24.60	1.54	40.8
24.60	1.56	41
24.70	1.57	41.5
24.70	1.6	41.8
24.70	1.5	43.3
24.70	1.53	45.3
24.70	1.54	46.2
24.80	1.58	44.7
24.80	1.55	43.3
24.80	1.51	42.5
24.80	1.54	41.7
24.80	1.55	41.8
24.90	1.57	42
24.90	1.57	41.5
24.90	1.55	41.5
24.90	1.56	42.5
24.90	1.56	44.7
25.00	1.56	48.8
25.00	1.6	54
25.00	1.74	53.5
25.00	1.55	46.4
25.00	1.54	41.8
25.10	1.53	40.6
25.10	1.56	41
25.10	1.59	41.7
25.10	1.58	41.4
25.10	1.6	40.6
25.20	1.56	39.3
25.20	1.59	38.6
25.20	1.57	38.1
25.20	1.56	38.7
25.20	1.59	40.2
25.30	1.53	42.7
25.30	1.57	45.9
25.30	1.54	45.4
25.30	1.55	44.6
25.30	1.57	45.2
25.40	1.59	44.4
25.40	1.54	42.2

25.40	1.54	41.8
25.40	1.52	43.9
25.40	1.63	47.8
25.50	1.57	48.3
25.50	1.62	45.6
25.60	1.58	40.2
25.60	1.56	41
25.60	1.55	41.9
25.60	1.58	42.3
25.70	1.6	42.1
25.70	1.54	40.9
25.70	1.58	40.2
25.70	1.56	39.9
25.70	1.56	39.2
25.80	1.56	39
25.80	1.56	39.2
25.80	1.58	39.7
25.80	1.57	40.3
25.80	1.57	40.2
25.90	1.57	40
25.90	1.54	40
25.90	1.58	40.6
25.90	1.57	40.4
25.90	1.58	39.9
26.00	1.55	39.1
26.00	1.55	39.1
26.00	1.56	39.7
26.00	1.58	40.7
26.00	1.58	41.2
26.10	1.56	40.7
26.10	1.56	40.2
26.10	1.54	40.3
26.10	1.53	41.5
26.10	1.56	43.9
26.20	1.6	45.4
26.20	1.56	44.4
26.20	1.57	44.6
26.20	1.59	46.1
26.20	1.62	47.4
26.30	1.63	47
26.30	1.56	44
26.30	1.56	42.5
26.30	1.58	42.7
26.30	1.6	43.8

26.40	1.6	46.1
26.40	1.63	49.6
26.40	1.55	49.1
26.40	1.58	47.6
26.40	1.62	49.5
26.50	1.56	48.1
26.50	1.56	43.3
26.50	1.56	40.5
26.50	1.57	39.5
26.50	1.58	40.1
26.60	1.58	42.3
26.60	1.64	43.4
26.60	1.59	42
26.60	1.58	41.6
26.60	1.56	42.5
26.70	1.62	42.7
26.70	1.56	40.6
26.70	1.58	39.4
26.70	1.59	38.8
26.70	1.55	38.2
26.80	1.58	38.3
26.80	1.59	39.1
26.80	1.59	38.8
26.80	1.58	38
26.80	1.58	38
26.90	1.56	38.2
26.90	1.57	38.6
26.90	1.57	38.9
26.90	1.57	39.7
26.90	1.59	40.3
27.10	1.56	39
27.10	1.55	39.9
27.10	1.57	42.2
27.10	1.62	44.8
27.10	1.54	43.9
27.20	1.54	43.4
27.20	1.61	45.9
27.20	1.64	45.9
27.20	1.57	43
27.20	1.55	40.8
27.30	1.56	39.4
27.30	1.56	38.8
27.30	1.56	39.3
27.30	1.57	39.7

27.30	1.56	39.4
27.40	1.56	39.3
27.40	1.56	39.3
27.40	1.56	39.5
27.40	1.52	39.9
27.40	1.54	40.3
27.50	1.58	40.4
27.50	1.55	39.3
27.50	1.54	38.5
27.50	1.55	38
27.50	1.53	38.5
27.60	1.53	39.2
27.60	1.53	42
27.60	1.56	45.5
27.60	1.59	45.6
27.60	1.61	44.3
27.70	1.56	41.8
27.70	1.57	40.2
27.70	1.58	39.5
27.70	1.56	39.3
27.70	1.58	38.9
27.80	1.55	38.5
27.80	1.58	38.8
27.80	1.58	39.1
27.80	1.55	39.2
27.80	1.57	39.7
27.90	1.58	40.2
27.90	1.56	40
27.90	1.59	40.5
27.90	1.61	41.6
27.90	1.62	42.8
28.00	1.61	43.6
28.00	1.63	44.2
28.00	1.58	42
28.00	1.59	39.7
28.00	1.58	38.6
28.10	1.58	38.1
28.10	1.58	37.8
28.10	1.57	37.7
28.10	1.58	37.7
28.10	1.59	37.4
28.20	1.57	37.3
28.20	1.58	36.9
28.20	1.6	36.9

28.20	1.56	37.2
28.20	1.5	37.3
28.30	1.52	37.4
28.30	1.56	38
28.30	1.56	39
28.30	1.58	40
28.30	1.58	40.9
28.40	1.57	42.1
28.40	1.63	43.9
28.40	1.55	45.9
28.40	1.54	45.2
28.40	1.55	40.9
28.60	1.56	45.5
28.60	1.57	42.1
28.60	1.58	39.5
28.60	1.6	39.4
28.70	1.6	40.8
28.70	1.55	41.7
28.70	1.57	40.1
28.70	1.59	39.3
28.70	1.6	41.5
28.80	1.61	45.8
28.80	1.6	47.3
28.80	1.58	44
28.80	1.59	42.1
28.80	1.58	40.8
28.90	1.56	40
28.90	1.58	
28.90	1.55	41.7
28.90	1.61	43.8
28.90	1.57	41.8
29.00	1.55	40
29.00	1.56	40
29.00	1.57	41.2
29.00	1.59	41.5
29.00	1.56	40.1
29.10	1.56	39.5
29.10	1.56	40.2
29.10	1.59	41.6
29.10	1.62	41.8
29.10	1.55	38.9
29.20	1.57	38.8
29.20	1.58	38.9
29.20	1.57	39.3

29.20	1.56	38.9
29.20	1.58	37.6
29.30	1.55	36.9
29.30	1.55	37.2
29.30	1.56	38.1
29.30	1.56	38.5
29.30	1.57	37.9
29.40	1.55	38
29.40	1.54	38.8
29.40	1.56	39.6
29.40	1.58	39
29.40	1.55	38.8
29.50	1.56	39
29.50	1.56	38.7
29.50	1.56	38.8
29.50	1.54	39.5
29.50	1.56	40.9
29.60	1.56	42.3
29.60	1.55	42.1
29.60	1.57	39.6
29.60	1.54	37.8
29.60	1.53	37.5
29.70	1.53	37.8
29.70	1.55	38.7
29.70	1.55	38.8
29.70	1.57	38.3
29.70	1.55	38.1
29.80	1.52	37.4
29.80	1.55	
29.80	1.52	37
29.80	1.53	38.2
29.80	1.58	39.7
29.90	1.55	38.8
29.90	1.41	36.9
29.90	1.45	36.4
29.90	1.49	37.7
29.90	1.5	40.1

Supplementary Table -2**Radiocarbon Ages**

Depth (mbsf)	Age (yr BP)	Error (y)
2.5	1486	47
97.5	4679	101
197.5	9584	31
292.5	10919	125
392.5	13539	131
492.5	14428	318
552.5	16834	252
592.5	17457	200
672.5	17800	360
692.5	18028	411
787.5	19855	304
892.5	20287	323
947.5	20924	311
1147.5	27647	447
1347.5	39326	1141
1547.5	41964	490
1747.5	47616	2141

Supplementary Table-3 : D₅₀ grain size data of the core MD161-29 (TrbZ = turbidite rich zone; HmpZ= Hemipelagic rich zone)

Depth (cmbsf)	Depositional Unit	D50) (µm	Depth (cmbsf)	Depositional Unit	D50 (µm)	Depth (cmbsf)	Depositional Unit	D50 (µm)
2.5	7.23	TrbZ	372.5	6.97	HmpZ	717.5	7.22	HmpZ
12.5	12.13	TrbZ	377.5	6.18	HmpZ	722.5	7.95	HmpZ
22.5	7.53	TrbZ	382.5	6.1	HmpZ	732.5	8.36	HmpZ
32.5	6.64	HmpZ	387.5	6.34	HmpZ	737.5	9.08	HmpZ
42.5	8.42	HmpZ	392.5	6.72	HmpZ	742.5	10.3	HmpZ
47.5	9.24	HmpZ	397.5	7.57	TrbZ	752.5	9.93	HmpZ
57.5	10.06	HmpZ	402.5	8.58	TrbZ	762.5	12.23	HmpZ
62.5	8.21	HmpZ	412.5	7.18	TrbZ	767.5	9.17	HmpZ
67.5	6.71	HmpZ	417.5	7.03	TrbZ	772.5	7.06	HmpZ
72.5	5.59	HmpZ	427.5	13.38	TrbZ	782.5	7.46	HmpZ
82.5	4.98	HmpZ	432.5	11.15	TrbZ	787.5	9.9	HmpZ
92.5	4.95	HmpZ	442.5	10.25	TrbZ	792.5	8.71	HmpZ
102.5	4.9	HmpZ	447.5	10.51	TrbZ	797.5	11.46	HmpZ
112.5	4.78	HmpZ	452.5	6.67	HmpZ	802.5	6.11	HmpZ
117.5	5.37	HmpZ	462.5	6.09	HmpZ	807.5	7.26	HmpZ
122.5	5.92	HmpZ	467.5	6.97	HmpZ	812.5	8.22	HmpZ
132.5	5.65	HmpZ	472.5	7.3	HmpZ	817.5	7.94	HmpZ
142.5	5.49	HmpZ	477.5	7.66	HmpZ	822.5	7.08	HmpZ
147.5	6.46	HmpZ	482.5	6.77	HmpZ	832.5	7.26	HmpZ
152.5	6.89	HmpZ	492.5	7.21	HmpZ	842.5	8.49	HmpZ
162.5	7.13	HmpZ	497.5	7.59	HmpZ	847.5	11.91	HmpZ
172.5	7.03	HmpZ	502.5	6.72	HmpZ	852.5	9.47	HmpZ
182.5	7.69	HmpZ	507.5	8.51	HmpZ	857.5	10.15	HmpZ
192.5	7.65	HmpZ	512.5	8.03	HmpZ	862.5	7.74	HmpZ
202.5	9.07	HmpZ	522.5	9.04	HmpZ	872.5	7.32	HmpZ
212.5	8.69	TrbZ	532.5	8.36	HmpZ	877.5	8.28	HmpZ
222.5	11.05	TrbZ	542.5	7.66	HmpZ	882.5	15.68	TrbZ
232.5	10.14	TrbZ	547.5	7.53	HmpZ	892.5	8.43	TrbZ
242.5	8.76	TrbZ	552.5	7.08	HmpZ	897.5	10.57	TrbZ
247.5	7.31	TrbZ	557.5	8.22	HmpZ	902.5	8.38	TrbZ
252.5	7.41	HmpZ	562.5	7.87	HmpZ	912.5	9.62	TrbZ
262.5	12.15	HmpZ	567.5	7.68	HmpZ	917.5	9.07	TrbZ
267.5	7.01	HmpZ	572.5	8.36	HmpZ	922.5	6.96	TrbZ
272.5	7.42	HmpZ	582.5	7.19	HmpZ	927.5	7.56	HmpZ
282.5	8.47	HmpZ	592.5	8.31	HmpZ	932.5	8.38	HmpZ
292.5	10.45	HmpZ	602.5	8.29	HmpZ	972.5	8.57	HmpZ
297.5	6.31	HmpZ	612.5	9.41	HmpZ	977.5	8.27	HmpZ
302.5	5.97	HmpZ	622.5	8.8	HmpZ	987.5	7.98	HmpZ
307.5	6.99	HmpZ	627.5	7.74	HmpZ	992.5	11.22	HmpZ
312.5	8.49	HmpZ	632.5	6.71	HmpZ	1002.5	10.98	HmpZ
322.5	11.03	HmpZ	642.5	7.98	HmpZ	1012.5	11.45	HmpZ

327.5	9.18	HmpZ	662.5	6.49	HmpZ	1022.5	10.59	HmpZ
332.5	12.11	HmpZ	672.5	7.85	HmpZ	1027.5	6.84	HmpZ
337.5	8.74	HmpZ	682.5	6.46	HmpZ	1032.5	7.86	HmpZ
342.5	9.49	HmpZ	687.5	7.13	HmpZ	1037.5	8.12	HmpZ
352.5	7.85	HmpZ	692.5	10.95	HmpZ	1042.5	7.34	HmpZ
357.5	8.91	HmpZ	702.5	8.31	HmpZ	1052.5	8.46	HmpZ
362.5	7.68	HmpZ	712.5	6.47	HmpZ	1062.5	9.18	HmpZ
Depth (cmbsf)	Depositional Unit	D50) (µm	Depth (cmbsf)	Depositional Unit	D50 (µm)	Depth (cmbsf)	Depositional Unit	D50 (µm)
1067.5	8.69	HmpZ	1482.5	7	HmpZ	1862.5	9.11	TrbZ
1077.5	9.61	TrbZ	1492.5	7.82	HmpZ	1867.5	9.29	TrbZ
1082.5	9.38	TrbZ	1497.5	7.52	HmpZ	1872.5	20.48	TrbZ
1092.5	8.39	TrbZ	1502.5	8.53	HmpZ	1877.5	9.42	TrbZ
1097.5	8.66	TrbZ	1512.5	8.28	HmpZ	1882.5	9.99	TrbZ
1102.5	11.15	TrbZ	1522.5	8.48	HmpZ	1892.5	15.48	TrbZ
1107.5	10.12	TrbZ	1527.5	7.07	HmpZ	1902.5	17.69	TrbZ
1117.5	8.66	TrbZ	1532.5	8.03	HmpZ	1907.5	9.22	TrbZ
1122.5	9.25	TrbZ	1542.5	9.49	HmpZ	1912.5	8.28	TrbZ
1127.5	6.93	TrbZ	1547.5	7.42	HmpZ	1917.5	9.15	TrbZ
1132.5	7.13	HmpZ	1552.5	8.21	HmpZ	1922.5	10.96	TrbZ
1147.5	8.63	HmpZ	1562.5	7.73	HmpZ	1927.5	22.42	TrbZ
1152.5	9.45	HmpZ	1607.5	7.33	HmpZ	1932.5	8.79	TrbZ
1162.5	8.42	HmpZ	1622.5	6.34	HmpZ	1937.5	9.94	TrbZ
1172.5	7.71	HmpZ	1632.5	7.22	HmpZ	1942.5	10.06	TrbZ
1192.5	8.54	HmpZ	1642.5	7.1	HmpZ	1947.5	13.45	TrbZ
1197.5	7.63	HmpZ	1647.5	8.73	HmpZ	1952.5	14.37	TrbZ
1202.5	10.95	HmpZ	1652.5	8.76	HmpZ	1962.5	9.28	TrbZ
1212.5	8.33	HmpZ	1657.5	7.8	TrbZ	1967.5	13.65	TrbZ
1222.5	9.39	HmpZ	1662.5	8.13	TrbZ	1972.5	9.32	TrbZ
1232.5	8.11	HmpZ	1667.5	10.43	TrbZ	1982.5	9.99	TrbZ
1247.5	9.73	HmpZ	1682.5	9.04	TrbZ	1987.5	12.5	TrbZ
1252.5	8.83	HmpZ	1687.5	13.69	TrbZ	1992.5	7.72	TrbZ
1272.5	8.19	HmpZ	1702.5	10.43	TrbZ	1997.5	13.03	TrbZ
1282.5	7.61	HmpZ	1707.5	8.42	TrbZ	2002.5	11.52	TrbZ
1292.5	8.92	HmpZ	1712.5	7.21	TrbZ	2007.5	13.02	TrbZ
1297.5	10.09	HmpZ	1717.5	9.33	TrbZ	2017.5	10.47	TrbZ
1307.5	9.52	HmpZ	1722.5	8.93	HmpZ	2022.5	9.38	TrbZ
1312.5	9.25	HmpZ	1727.5	8.72	HmpZ	2027.5	10.3	TrbZ
1322.5	7.1	HmpZ	1732.5	7.22	HmpZ	2032.5	8.46	TrbZ
1327.5	7.54	HmpZ	1742.5	7.27	HmpZ	2042.5	7.94	TrbZ
1332.5	8.88	HmpZ	1747.5	7.68	HmpZ	2052.5	8.3	TrbZ
1347.5	8.4	HmpZ	1752.5	7.36	HmpZ	2062.5	8.21	TrbZ
1352.5	13.84	HmpZ	1762.5	6.99	HmpZ	2077.5	8.38	TrbZ
1362.5	7.59	HmpZ	1772.5	9.9	HmpZ	2082.5	8.1	TrbZ

1372.5	8.09	HmpZ	1777.5	6.82	HmpZ	2092.5	7.15	HmpZ
1382.5	6.78	HmpZ	1782.5	7.73	TrbZ	2097.5	8.05	HmpZ
1392.5	7.25	HmpZ	1792.5	8.29	TrbZ	2102.5	8.27	HmpZ
1402.5	7.54	HmpZ	1802.5	8	TrbZ	2112.5	8.22	HmpZ
1412.5	8.3	HmpZ	1807.5	8.29	TrbZ	2122.5	7.97	HmpZ
1417.5	8.78	HmpZ	1812.5	8.99	TrbZ	2132.5	8.02	HmpZ
1422.5	7.31	HmpZ	1817.5	10.76	TrbZ	2142.5	7.41	HmpZ
1432.5	8.79	HmpZ	1827.5	8.39	TrbZ	2147.5	7.95	TrbZ
1442.5	7.85	HmpZ	1837.5	10.45	TrbZ	2152.5	8.31	TrbZ
1452.5	7.66	HmpZ	1842.5	14.58	TrbZ	2162.5	10.77	TrbZ
1457.5	8.08	HmpZ	1847.5	12.83	TrbZ	2167.5	8.49	TrbZ
1462.5	8.46	HmpZ	1852.5	12.46	TrbZ	2172.5	7.98	TrbZ
1472.5	6.89	HmpZ	1857.5	9.11	TrbZ	2187.5	13.25	TrbZ
Depth (cmbsf)	Depositional Unit	D50) (µm	Depth (cmbsf)	Depositional Unit	D50 (µm)	Depth (cmbsf)	Depositional Unit	D50 (µm)
2192.5	9.94	TrbZ	2572.5	8.86	HmpZ	2982.5	9.3	HmpZ
2197.5	7.28	TrbZ	2577.5	8.67	HmpZ	2992.5	9.95	TrbZ
2202.5	7.88	TrbZ	2592.5	7.73	TrbZ	2997.5	16.8	TrbZ
2207.5	8.1	TrbZ	2597.5	7.65	TrbZ			
2217.5	18.82	TrbZ	2602.5	9.66	TrbZ			
2222.5	8.26	TrbZ	2612.5	8.93	TrbZ			
2227.5	8.5	TrbZ	2617.5	8.64	TrbZ			
2232.5	9.09	TrbZ	2622.5	9.38	TrbZ			
2237.5	9.59	TrbZ	2632.5	10.27	TrbZ			
2242.5	8.81	TrbZ	2637.5	10.6	TrbZ			
2247.5	7.83	TrbZ	2647.5	8.2	TrbZ			
2252.5	9.6	TrbZ	2652.5	8.45	TrbZ			
2257.5	7.13	HmpZ	2657.5	8.44	HmpZ			
2262.5	8.66	HmpZ	2677.5	8.3	HmpZ			
2272.5	9.04	HmpZ	2687.5	8.36	HmpZ			
2277.5	8.26	HmpZ	2697.5	8.38	HmpZ			
2287.5	9.36	HmpZ	2702.5	8.4	HmpZ			
2297.5	9.06	HmpZ	2707.5	8.42	HmpZ			
2307.5	7.37	HmpZ	2712.5	9.31	HmpZ			
2317.5	9.08	HmpZ	2717.5	8.84	TrbZ			
2332.5	9.5	HmpZ	2747.5	8.75	TrbZ			
2342.5	8.82	HmpZ	2752.5	8.95	TrbZ			
2352.5	9.02	TrbZ	2757.5	15.33	TrbZ			
2362.5	9.2	TrbZ	2762.5	13.05	TrbZ			
2367.5	8.3	TrbZ	2772.5	8.82	TrbZ			
2382.5	8.46	TrbZ	2782.5	8.74	HmpZ			
2397.5	7.75	HmpZ	2792.5	10.56	HmpZ			
2402.5	9.71	HmpZ	2802.5	8.52	HmpZ			
2412.5	8.91	HmpZ	2812.5	8.51	HmpZ			

2417.5	8.52	HmpZ	2822.5	9.01	TrbZ			
2427.5	8.44	TrbZ	2837.5	13.17	TrbZ			
2437.5	10	TrbZ	2847.5	9.86	TrbZ			
2442.5	10.96	TrbZ	2852.5	16.27	TrbZ			
2447.5	8.81	TrbZ	2857.5	8.84	TrbZ			
2452.5	8.55	TrbZ	2862.5	10.01	TrbZ			
2462.5	8.47	TrbZ	2872.5	11.33	HmpZ			
2472.5	8.64	TrbZ	2877.5	8.92	HmpZ			
2477.5	8.15	TrbZ	2882.5	9.03	HmpZ			
2482.5	10.36	TrbZ	2887.5	9.61	HmpZ			
2487.5	9.46	TrbZ	2892.5	8.64	HmpZ			
2497.5	17	TrbZ	2907.5	8.69	HmpZ			
2502.5	9.4	TrbZ	2912.5	8.56	HmpZ			
2512.5	10.2	TrbZ	2922.5	7.76	HmpZ			
2527.5	10.21	TrbZ	2932.5	8.62	HmpZ			
2532.5	8.77	HmpZ	2942.5	8.82	HmpZ			
2542.5	9.02	HmpZ	2952.5	9.31	HmpZ			
2552.5	9.62	HmpZ	2962.5	8.47	HmpZ			
2562.5	9.4	HmpZ	2972.5	8.41	HmpZ			

Supplementary Table -4:
CaCO₃, TOC (wt%), (TOC/TN)_{molar} and δ¹³C_{TOC} data of the core MD161/29

Depth (cmbsf)	CaCO ₃ (wt%)	TOC (wt%)	(TOC/TN) _{molar}	δ ¹³ C ‰ (VPDB)
2.5	3.67	0.63	15.94	-19.6
12.5	3.23	0.52	9.64	-20.9
22.5	3.34	0.62	9.45	-19.9
32.5	4.26	0.60	10.21	-20.6
42.5	4.29	0.56	9.56	-20.1
47.5	3.60	0.58	10.42	-20.8
52.5	3.77	0.53	11.6	-21.1
62.5	3.63	0.57	10.68	-21.4
72.5	4.86	0.60	9.76	-20.6
82.5	6.31	0.61	9.47	-21.3
92.5	8.26	0.60	8.86	-21.0
97.5				-21.0
102.5	8.73	0.66	9.63	-20.7
112.5	7.47	0.61	9.29	-21.3
122.5	4.43	0.55	9.83	-20.9
132.5	6.55	0.54	9.25	-21.3
142.5	6.09	0.51	10.97	-20.8
147.5	5.92	0.52	9.52	-20.9
152.5				-21.3
162.5	4.68	0.50	10.16	-20.8
172.5	4.66	0.46	9.42	-20.9
182.5	4.43	0.54	11.85	-20.7
192.5	3.31	0.45	12.54	-21.1
202.5	5.50	0.54	11	-21.1
212.5	9.24	0.66	12.34	-21.1
222.5	6.05	0.54	12.1	-21.3
232.5	6.04	0.54	12.49	-21.0
242.5				-20.9
252.5	5.04	0.46	9.79	-20.6
262.5	6.90	0.35	12.79	-21.1
272.5	4.82	0.44	11.08	-20.7
282.5	7.18	0.50	9.62	-20.7
292.5	9.42	0.43	9.83	-21.0
302.5	7.77	0.49	9.76	-20.0
312.5	6.39	0.47	11	-20.3
322.5	6.44	0.46	11.36	-20.6

332.5	5.62	0.47	10.96	-20.7
342.5	6.49	0.56	13.21	-20.6
352.5	6.17	0.38	8.11	-20.3
362.5	10.16	0.47	12.34	-19.6
372.5	9.50	0.52	11.27	-20.0
382.5	10.60	0.58	11.61	-19.9
392.5	6.79	0.49	10.51	-19.8
402.5	6.80	0.41	9.73	-19.7
412.5	6.91	0.47	11.12	-19.1
422.5	5.31	0.46	11.26	-19.2
432.5	7.33	0.46	12.41	-19.2
442.5	4.72	0.41	11.06	-18.6
452.5	7.88	0.56	12.34	-19.1
462.5	9.34	0.36	8.08	-18.5
467.5	6.53	0.41	10.92	-19.2
472.5	7.59	0.25	6.11	-18.9
477.5	9.07	1.31	18.1	-19.0
482.5	8.13	0.55	12.93	-18.7
492.5	6.33	0.50	11.63	-19.0
502.5	3.83	0.57	8.73	-19.1
512.5	8.23	0.42	9.98	-18.8
522.5	7.78	0.39	11.6	-18.9
532.5	6.54	0.58	16.55	-19.5
542.5	5.84	0.47	11.4	-18.3
552.5	4.97	0.57	10.71	-18.9
562.5	6.97	0.46	10.53	-18.6
572.5	5.77	0.49	12.47	-18.7
582.5	6.36	0.40	9.78	-18.6
592.5	4.46	0.52	12.86	-19.5
602.5	6.52	0.45	11.98	-19.4
612.5	6.14	0.44	12.75	-18.5
622.5	5.80	0.48	15	-18.8
632.5	7.40	0.52	11.3	-18.8
642.5	6.67	0.49	11.74	-19.0
652.5	6.27	0.48	13.16	-18.6
662.5	6.37	0.54	11.24	-18.9
672.5	5.00	0.58	11.87	-19.0
682.5	8.78	0.54	13.34	-19.2
692.5	4.77	0.42	11.7	-18.9
702.5	6.08	0.43	11.14	-18.0
712.5	6.11	0.48	11.69	
722.5	5.44	0.50	15.99	-18.5

732.5	5.47	0.40	12.65	
742.5	5.05	0.40	16.09	
752.5	4.81	0.49	16.52	-18.7
762.5	5.70	0.42	15.52	-18.0
772.5	5.50	0.48	11.58	-18.4
782.5	5.73	0.39	11.13	-18.3
792.5	5.40	0.43	12.89	-18.1
797.5				-18.3
802.5	10.12	0.58	11.93	-18.0
812.5	5.88	0.45	10.84	-18.7
822.5	6.77	0.50	11.74	-18.6
832.5	5.47	0.49	10.45	-18.4
842.5	5.11	0.47	12.69	-18.9
847.5	5.66	0.36	12.02	-19.0
852.5	5.70	0.41	12.63	-18.6
862.5	8.54	0.41	8.71	-19.3
872.5	5.49	0.49	12.97	-19.2
882.5	5.81	0.34	10.4	-18.5
892.5	5.29	0.51	11.8	-19.5
897.5				-18.9
902.5	7.04	0.25	11.24	-19.3
912.5	4.49	0.50	12.38	-19.7
922.5	9.09	0.45	9.94	-19.2
932.5	4.73	0.56	12.81	-18.9
	7.44	0.60	11.88	
952.5	5.32	0.43	12.67	-19.0
962.5	5.04	0.46	12.61	-18.8
972.5	6.02	0.48	16.54	-18.8
982.5	5.09	0.44	11.39	-18.5
992.5	4.54	0.46	11.37	-18.6
1002.5	6.13	0.59	11.56	-19.2
1012.5	5.68	0.45	10.98	-18.6
1022.5	7.49	0.46	10.93	-18.7
1032.5	7.59	0.55	11.27	-19.1
1042.5	6.69	0.61	11.81	-18.9
1052.5	4.43	0.49	12.4	-19.3
1062.5	8.00	0.69	12.6	-19.4
1072.5	4.23	0.62	11.81	-19.5
1082.5	4.44	0.50	11.14	-19.4
1092.5	3.28	0.44	10.34	-19.2
1102.5	3.53	0.44	10.61	-19.0
1112.5	6.06	0.51	10.57	-19.3

1122.5	5.80	0.42	11.31	-19.5
1132.5	3.41	0.93	18.02	-19.2
1142.5	5.39	0.54	11.6	-19.0
1147.5				
1152.5	5.93	0.54	11.07	-19.5
1162.5	5.97	0.53	13.54	-19.1
1172.5	6.72	0.42	10.78	-19.1
1182.5	5.51	0.58	11.53	-19.4
1192.5	3.89	0.59	12.55	-20.2
1202.5	6.18	0.63	10.58	-19.4
1212.5	5.30	0.43	10.53	-19.9
1222.5	6.06	0.56	12.84	-18.7
1232.5	5.81	0.54	13.83	-18.5
1242.5	4.96	0.42	11.59	-18.4
1252.5	4.70	0.51	14.99	-18.3
1262.5	3.95	0.45	12.28	-18.2
1272.5	10.54	0.42	9.99	-18.2
1282.5	11.26	0.72	14.87	-17.9
1292.5	6.43	0.47	13.04	-18.6
1302.5	4.84	0.50	13.5	-18.3
1312.5	4.16	0.62	16.51	-19.1
1322.5	7.54	0.55	12.92	-18.4
1332.5	5.16			-18.6
1342.5	5.99	0.58	13.62	-18.9
1347.5				
1352.5	4.01	0.42	11.7	-18.4
1362.5	5.15	0.42	10.48	-18.5
1372.5	6.54	0.43	9.46	-20.1
1382.5	5.77	0.76	14.83	-19.0
1392.5	7.26	0.69	10.73	-18.9
1402.5	3.62	0.71	15.72	-19.2
1412.5	4.52	0.41	8.85	-18.3
1422.5	5.47	0.50	12.69	-18.9
1432.5	3.56	0.52	11.33	-19.0
1442.5	4.61	0.51	12.39	-18.8
1452.5	6.82	0.45	10.52	-18.8
1457.5				-19.1
1462.5	3.76	0.51	11.02	-19.1
1472.5	6.01	0.88	10.92	-18.5
1482.5	5.02	0.96	15.84	-18.3
1492.5	5.59	0.85	11.37	-19.5
1502.5	3.63	0.91	11.36	-19.7

1512.5	3.91	0.63	10.13	-19.5
1522.5	5.21	0.71	11.88	-19.6
1532.5	4.27	0.60	9.49	-20.0
1542.5	4.98	0.51	10.92	-19.8
1547.5				
1552.5	2.44	0.87	17.68	-18.8
1562.5	4.88	0.62	10.57	-19.4
1607.5	3.13	0.78	13.89	-18.9
1622.5	3.67	0.63	11.22	-19.8
1632.5	6.25	0.60	11.6	-19.5
1642.5	7.49	0.75	16.13	-18.6
1647.5				
1652.5	4.57	0.65	13.76	-19.7
1662.5	2.54	0.79	17.07	-20.3
1672.5	4.84	0.64	12.65	-20.3
1682.5				-18.5
1687.5	4.80	0.50	11.75	-19.8
1692.5				
1702.5	3.91	0.47	20.6	-20.1
1712.5	4.08			
1717.5	5.24	0.52	11.54	-19.4
1722.5				-18.2
1732.5	5.06	1.48	18.71	-19.7
1742.5				
1747.5				
1752.5	6.59	0.65	10.57	-19.1
1762.5				
1772.5	5.34	0.47	13.59	-19.0
1782.5				
1792.5	5.60	0.43	12.54	-19.2
1802.5	5.23	0.46	9.99	-19.4
1817.5	3.61	0.69	19.37	-20.5
1832.5	4.20	0.55	19.44	-20.6
1847.5	6.00	0.44	12.66	-21.0
1852.5				
1862.5	4.77	0.57	12.94	-20.7
1872.5				
1877.5	4.98	0.53	19.58	-21.0
1882.5				-19.2
1892.5	5.68	0.47	13.65	-21.0
1902.5	5.38	0.42	13.15	-20.8
1912.5	5.82	0.40	14.42	-20.9
1927.5	4.78	0.54	20.57	-21.2
1932.5	4.00	0.62	15.02	-20.3

1942.5	5.46	0.42	13.75	-20.4
1952.5				-20.7
1962.5	4.29	0.51	18.23	-20.6
1967.5	3.64	0.55	10.96	-20.5
1972.5	5.52	0.26	6.23	-21.8
1982.5	4.40	0.51	12.66	-20.7
1987.5	4.66	0.51	16.87	-20.2
1992.5	4.63	0.60	12.86	-20.3
1997.5				-20.4
2002.5	5.26	0.55	15.07	-21.1
2007.5				
2012.5	5.45	0.49	11.75	-20.6
2017.5				-20.7
2022.5	5.08	0.47	10.98	-21.3
2027.5				
2032.5	5.14	0.43	12.14	-21.7
2037.5	5.32	0.53	14.54	-20.3
2042.5	5.66	0.51	12.74	-20.8
2047.5				-20.4
2052.5	5.45	0.48	12.16	-20.6
2057.5				-20.4
2062.5	5.74	0.46	13.81	-20.8
2067.5				-20.7
2077.5	5.27	0.52	11.83	-20.7
2082.5				-20.3
2092.5				
2097.5	4.94	0.51	12.72	-20.5
2102.5	3.23	0.62	13.34	-20.4
2112.5	4.30	0.55	11.42	-20.4
2117.5				-20.4
2122.5	4.04	0.56	12.7	-20.5
2132.5	4.01	0.51	10.24	-20.7
2142.5	3.32	0.46	11.9	-21.3
2147.5	3.83	0.52	10.49	-20.2
2152.5	4.16	0.43	10.02	-20.6
2162.5	4.48	0.44	12.04	-20.8
2167.5	4.04	0.49	11.9	-20.8
2172.5	4.16	0.43	10.3	-20.3
2182.5				
2187.5	4.15	0.33	10.74	-20.7
2197.5	3.94	0.50	12.23	-20.7
2207.5	4.52	0.49	11.36	-20.5
2217.5	4.35	0.50	12.36	-21.0
2232.5	4.84	0.46	13.28	-20.4

2242.5	4.81	0.51	11.75	-20.6
2247.5	4.45	0.53	11.41	-20.3
2252.5	5.06	0.43	11.96	-20.4
2257.5	4.06	0.55	11.79	-20.7
2262.5	2.07	0.80	17.97	-20.9
2272.5				
2277.5	3.64	0.51	10.12	-21.0
2287.5				
2297.5	3.66	0.56	12.11	-20.7
2307.5				
2317.5	4.14	0.55	12.14	-20.1
2322.5				
2332.5	4.58	0.47	11.99	-20.1
2342.5	5.11	0.45	9.82	-20.2
2352.5				-20.0
2362.5				
2367.5	4.32	0.57	12.6	-21.7
2382.5	4.28	0.54	11.41	-20.3
2397.5	4.66	0.46	12.62	-20.1
2402.5	4.25	0.56	11.55	-20.3
2412.5	3.93	0.52	12.39	-21.5
2417.5	4.79	0.50	11.35	-20.7
2427.5				
2437.5				-20.7
2442.5	4.46	0.51	11.35	-20.8
2452.5	4.64	0.47	13.55	-20.2
2462.5	4.43	0.52	11.4	-20.8
2472.5	4.18	0.56	12.59	-20.5
2482.5	4.63	0.51	11.65	-20.8
2492.5	4.40	0.50	12.92	-20.9
2502.5	4.77	0.51	11.48	-20.6
2512.5	4.61	0.53	11.97	-20.7
2522.5	4.08	0.63	12.74	-20.9
2527.5	3.49	0.59	12.96	-20.5
2532.5	4.10	0.51	13.99	-20.4
2542.5	4.50	0.51	12.34	-20.7
2552.5	3.43	0.64	13.65	-20.6
2562.5	4.35	0.45	12.12	-20.5
2572.5	3.09	0.53	13.55	-20.7
2577.5	4.78	0.45	10.45	-20.6
2592.5	4.37	0.48	10.63	-20.4
2597.5	3.69	0.59	11.45	-20.3
2602.5	4.00	0.52	12.41	-20.3
2612.5	3.25	0.57	10.87	-20.5

2617.5				-19.9
2622.5	3.97	0.50	14.2	-20.7
2632.5	3.70	0.55	13.1	-21.0
2637.5	3.59	0.56	13	-20.7
2647.5				-20.1
2652.5	3.85	0.52	12.13	-20.3
2657.5	3.57	0.55	15.83	-20.0
2677.5	3.99	0.54	11.3	-20.7
2687.5				
2697.5	3.58	0.56	10.87	-20.3
2702.5				
2707.5	4.13	0.53	10.91	-20.3
2712.5				
2717.5	3.22	0.61	12.79	-20.1
2732.5	4.07	0.60	13.38	-20.4
2747.5	3.75	0.55	11.9	-20.4
2762.5	4.41	0.58	14.74	-20.5
2772.5	4.92	0.40	9.33	-20.5
2782.5	4.01	0.54	12.92	-20.5
2792.5	4.69	0.45	11.95	-20.5
2802.5	4.45	0.54	10.97	-20.2
2812.5				
2822.5	4.34	0.61	13.65	-20.3
2837.5	4.61	0.50	12.66	-20.6
2847.5				
2852.5	4.29	0.57	13.56	-21.0
2862.5	5.13	0.39	11.21	-20.3
2872.5	3.10	0.64	15.58	-20.7
2882.5	3.90	0.56	14.65	-20.3
2892.5	5.03	0.45	9.94	-20.1
2907.5	3.28	0.57	11.81	-20.7
2912.5	4.42	0.49	11.04	-20.2
2922.5	4.44	0.53	12.64	-20.3
2932.5	4.09	0.52	14.11	-20.0
2942.5	4.34	0.45	12.97	-20.3
2952.5	4.74	0.45	14.74	-20.4
2962.5	4.26	0.52	15.36	-20.1
2972.5	4.85	0.47	14.24	-20.2
2982.5	5.10	0.39	13.9	-20.3
2992.5				
2997.5	4.32	0.42	9.72	-20.9

Supplementary Table-5. Contents of AVS (wt%), CRS (wt%), S⁰ (wt%), TRIS (wt%), FePy (wt%), Fe_{AVS} (wt%), Fe_{Mag} (wt%), Fe_D (wt%), Fe_{Ox} (wt%), and Fe_{TR}(wt%); Sulfur ($\delta^{34}\text{S}_{\text{CRS}}$ and $\delta^{34}\text{S}_{\text{AVS}}$) isotope ratios measured in the core MD161/29 along the depth.

Depth (cmbsf)	AVS (wt%)	CRS (wt%)	S ⁰ (wt %)	TRIS (wt%)	$\delta^{34}\text{S}_{\text{AVS}}$ (‰VCDT)	$\delta^{34}\text{S}_{\text{CRS}}$ (‰VCDT)	Fe _{Py} (wt%)	Fe _{AVS} (wt%)	Fe _{Mag} (wt%)	Fe _D (wt%)	Fe _{Ox} (wt%)	Fe _{TR} (wt%)
2.5	0.011	0.0012	0.012			-4.4	0.009		0.85	0.77	0.77	1.63
12.5	0.002		0.002			-9.5	0.002		0.74	0.58	0.58	1.33
22.5									0.72	0.76	0.76	
32.5	0.003		0.003			2.8	0.002		0.22	0.78	0.78	1.00
42.5									0.68	0.57	0.57	
47.5	0.003		0.003			-8.8	0.003		0.14	0.58	0.58	0.72
52.5												
62.5									0.18	0.5	0.5	
72.5	0.005		0.005			-4.1	0.004		0.15	0.63	0.63	0.78
82.5									0.78	0.48	0.48	
92.5												
97.5	0.008		0.008			-5.7	0.007		0.71	0.47	0.47	1.19
102.5										0.49	0.49	
112.5									0.69	0.5	0.5	
122.5	0.003		0.003			-7.5	0.003		0.69	0.67	0.67	1.37
132.5									0.05	0.5	0.5	
142.5									0.59	0.51	0.51	
147.5	0.009		0.009			-18.5	0.008		0.18	0.96	0.96	1.14
152.5									0.69	0.66	0.66	
162.5									0.17	0.55	0.55	
172.5	0.010		0.010			-10.0	0.009		0.09	0.61	0.61	0.71
182.5	0.010		0.010			-9.1	0.009		0.12	0.66	0.66	0.79
192.5	0.011		0.011			-4.6	0.009		0.16	0.78	0.78	0.95
202.5	0.012		0.012			2.7	0.010		0.96	0.76	0.76	1.73
212.5	0.013	0.006	0.019			-36.6	0.011		0.93	0.7	0.7	1.64
222.5									0.19	0.86	0.86	
232.5	0.008		0.008			-21.1	0.007		0.74	0.77	0.77	1.52
242.5									0.11	0.65	0.65	
252.5									0.18	0.66	0.66	
262.5	0.001		0.001			-23.2	0.001		0.69	0.56	0.56	1.25
272.5									0.24	0.72	0.72	
282.5									0.76	0.7	0.7	
292.5									0.69	0.62	0.62	
302.5	0.006		0.006			-44.5	0.005		0.94	0.63	0.63	1.57
312.5									0.74	0.6	0.6	
322.5	0.007		0.007			-18.5	0.006		0.14	0.56	0.56	0.70
332.5									0.19	0.56	0.56	
342.5	0.004		0.004			-35.3	0.004		0.12	0.7	0.7	0.83

352.5								0.27	0.87	0.87	
362.5	0.021		0.021		-39.4	0.018		0.73	0.66	0.66	1.40
372.5								0.18	0.81	0.81	
382.5	0.008		0.008		-45.2	0.007		0.19	0.72	0.72	0.91
392.5	0.005		0.005		-47.6	0.004		0.25	0.82	0.82	1.08
402.5								0.19	0.7	0.7	
412.5	0.006		0.006		-45.7	0.005		0.21	0.83	0.83	1.04
422.5								0.19	0.82	0.82	
432.5								0.19	0.59	0.59	
442.5	0.008		0.008		-41.2	0.007		0.13	0.8	0.8	0.94
452.5	0.004		0.004		-33.8	0.003		0.81			
462.5								0.22			
467.5								1.04	0.78	0.78	
472.5	0.004		0.004		-40.8	0.003		0.94	0.79	0.79	1.73
477.5								0.26	0.79	0.79	
482.5								1.06	0.71	0.71	
492.5	0.004		0.004		-39.0	0.003		0.13	1	1	1.13
502.5								1.29	0.82	0.82	
512.5	0.001		0.001		-39.5	0.001		0.21	0.67	0.67	0.88
522.5								0.32	0.71	0.71	
532.5	0.002		0.002		-43.2	0.001		0.12	0.71	0.71	0.83
542.5	0.016		0.016		-45.5	0.014		1.29	0.67	0.67	1.98
552.5								1.09	0.75	0.75	
562.5	0.026		0.026		-46.7	0.022		1.05	0.66	0.66	1.73
572.5								1.24	0.64	0.64	
582.5								1.13	0.65	0.65	
592.5	0.017		0.017		-24.6	0.015		0.15	0.76	0.76	0.92
602.5	0.032		0.032		-43.0	0.028		0.80	0.73	0.73	1.56
612.5	0.018		0.018		-45.9	0.015		0.12	0.74	0.74	0.87
622.5								0.20	0.67	0.67	
632.5	0.036		0.036		-47.1	0.032		1.22	0.66	0.66	1.91
642.5	0.033		0.033		-44.8	0.029		1.11	0.6	0.6	1.74
652.5								0.22	0.72	0.72	
662.5	0.055		0.055		-47.0	0.048		1.03	0.72	0.72	1.80
672.5								1.22	0.7	0.7	
682.5	0.043		0.043		-46.4	0.038		0.14	0.79	0.79	0.96
692.5								0.30	0.73	0.73	
702.5	0.046		0.046		-46.0	0.040		0.12	0.74	0.74	0.90
712.5								1.08	0.7	0.7	
722.5	0.013		0.013		-38.9	0.012		0.92	0.69	0.69	1.62
732.5									0.6	0.6	
742.5								0.22	0.71	0.71	
752.5	0.017		0.017		-33.7	0.015		1.17	0.67	0.67	1.86
762.5								0.19	0.58	0.58	

772.5		0.031		0.031		-47.1	0.027		0.96	0.64	0.64	1.62
782.5									0.12	0.38	0.38	
792.5									0.77	0.64	0.64	
797.5		0.006		0.006		-35.4	0.005		0.78	0.48	0.48	1.27
802.5									0.97	0.54	0.54	
812.5									1.01	0.87	0.87	
822.5		0.064		0.064		-44.7	0.055		0.64	0.59	0.59	1.28
832.5									0.26	0.77	0.77	
842.5									0.20	0.62	0.62	
847.5									0.13	0.59	0.59	
852.5									0.22	1.04	1.04	
862.5		0.032		0.032		-44.1	0.028		0.74	0.56	0.56	1.33
872.5									0.25	0.76	0.76	
882.5		0.103		0.103		-22.5	0.089		1.01	0.48	0.48	1.58
892.5									0.69	0.62	0.62	
897.5									0.13	0.61	0.61	
902.5									0.67	0.48	0.48	
912.5		0.058		0.058		-31.4	0.051		0.24			
922.5									0.91	0.52	0.52	
932.5		0.080		0.080		-43.4	0.070		0.90	0.62	0.62	1.59
									0.66	0.66		
952.5		0.038		0.038		-40.9	0.033		0.67	0.42	0.42	1.13
962.5									0.25	0.74	0.74	
972.5		0.027		0.027		-41.6	0.023		0.76	0.5	0.5	1.29
982.5												
992.5		0.080		0.080		-43.0	0.070		0.23	0.63	0.63	0.93
1002.5		0.056		0.056		-39.0	0.049		0.29	0.66	0.66	1.00
1012.5									0.93	0.49	0.49	
1022.5		0.096		0.096		-44.4	0.084		0.90	0.58	0.58	1.57
1032.5									1.28	0.58	0.58	
1042.5		0.055		0.055		-43.8	0.048		1.07	0.5	0.5	1.62
1052.5									0.20	0.58	0.58	
1062.5		0.072		0.072		-43.3	0.063		0.98	0.59	0.59	1.63
1072.5												
1082.5		0.048		0.048		-42.5	0.042		0.12	0.7	0.7	0.87
1092.5									0.24	0.7	0.7	
1102.5		0.043		0.043		-29.2	0.037			0.58	0.58	
1112.5		0.073		0.073		-45.1	0.064					
1122.5									0.23	0.53	0.53	
1132.5		0.104		0.104		-44.6	0.091		0.12	0.74	0.74	0.96
1142.5									0.21	0.56	0.56	
1147.5												
1152.5		0.088	0.003	0.091		-43.5	0.077		0.65	0.61	0.61	1.34
1162.5									0.82	0.54	0.54	

1172.5		0.047	0.013	0.060		-39.2	0.041		0.96	0.55	0.55	1.55
1182.5									0.23	0.67	0.67	
1192.5		0.034		0.034		-34.7	0.030		1.02	0.62	0.62	1.67
1202.5		0.136		0.136		-45.4	0.118		0.17	0.65	0.65	0.93
1212.5									0.22	0.49	0.49	
1222.5		0.095		0.095		-42.8	0.083		1.01	0.62	0.62	1.71
1232.5									0.79	0.65	0.65	
1242.5		0.100		0.100		-43.5	0.087		0.80	0.65	0.65	1.54
1252.5									0.25	0.61	0.61	
1262.5		0.047		0.047		-43.0	0.041		1.14	0.5	0.5	1.68
1272.5									0.18	0.49	0.49	
1282.5		0.070	0.068	0.138		-44.1	0.061		0.93	0.69	0.69	1.68
1292.5		0.110		0.110		-44.9	0.096		0.13	0.64	0.64	0.86
1302.5									0.97	0.55	0.55	
1312.5		0.059	0.001	0.060		-41.9	0.052		0.36	0.66	0.66	1.07
1322.5									0.97	0.53	0.53	
1332.5									0.23	0.61	0.61	
1342.5		0.129	0.008	0.138		-40.9	0.113		0.15	0.59	0.59	0.85
1347.5												
1352.5									0.72	0.56	0.56	
1362.5		0.024	0.001	0.025		-44.2	0.021		1.12	0.64	0.64	1.78
1372.5									1.01			
1382.5		0.051		0.051		-45.3	0.045		0.25	0.57	0.57	0.87
1392.5									0.75	0.5	0.5	
1402.5		0.079		0.079		-44.5	0.069		0.14	0.69	0.69	0.90
1412.5									0.20	0.68	0.68	
1422.5		0.045		0.045		-39.1	0.039		0.83	0.6	0.6	1.47
1432.5									0.21	0.54	0.54	
1442.5		0.139	0.025	0.164		-41.2	0.121		0.12	0.62	0.62	0.86
1452.5		0.065		0.065		-38.3	0.056		0.79	0.58	0.58	1.42
1457.5												
1462.5									0.27	0.62	0.62	
1472.5		0.136		0.136		-42.3	0.118		0.13	0.63	0.63	0.87
1482.5									0.70	0.47	0.47	
1492.5		0.160		0.160		-42.6	0.139		0.13	0.54	0.54	0.81
1502.5									0.65	0.47	0.47	
1512.5		0.056		0.056		-37.7	0.049		0.19	0.66	0.66	0.90
1522.5									1.07	0.57	0.57	
1532.5									0.72	0.59	0.59	
1542.5									0.85	0.58	0.58	
1547.5												
1552.5		0.012		0.012		-37.2	0.011		1.18	0.64	0.64	1.83
1562.5									0.13	0.63	0.63	
1607.5		0.096		0.096		-45.3	0.083		0.96			

1622.5									0.12	0.57	0.57	
1632.5									0.22	0.7	0.7	
1642.5	0.063		0.063		-43.9	0.055		0.90	0.53	0.53	1.49	
1647.5												
1652.5									0.22	0.77	0.77	
1662.5	0.028	0.015	0.043		-46.1	0.024		0.96	0.58	0.58	1.56	
1672.5									0.24	0.65	0.65	
1682.5									0.22	0.63	0.63	
1687.5	0.027		0.027		-31.2	0.023		0.80	0.59	0.59	1.41	
1692.5									0.20	0.62	0.62	
1702.5	0.021	0.002	0.022		-23.3	0.018		0.97	0.44	0.44	1.43	
1712.5									0.79	0.62	0.62	
1717.5	0.037		0.037		-43.7	0.032		1.04	0.81	0.81	1.88	
1722.5									0.96	0.73	0.73	
1732.5	0.032		0.032		-36.9	0.028		1.05	0.63	0.63	1.71	
1742.5									0.90	0.56	0.56	
1747.5												
1752.5	0.012		0.012		-43.7	0.010		0.20	0.6	0.6	0.81	
1762.5									1.30	0.68	0.68	
1772.5	0.040	0.014	0.054		-40.6	0.035		0.27				
1782.5									1.21			
1792.5	0.014		0.014		-38.4	0.012		0.24	0.73	0.73	0.98	
1802.5	0.020	0.003	0.023		-38.1	0.018		0.15	0.76	0.76	0.93	
1817.5	0.006	0.070		0.076	-37.0	-28.5	0.061	0.01	0.60	0.75	0.74	1.41
1832.5	0.037	0.058		0.095	-36.8	-26.4	0.051	0.07	0.15	1.06	0.99	1.26
1847.5	0.007	0.036	0.033	0.076	-37.2	-24.7	0.032	0.01	0.78	0.85	0.84	1.66
1852.5									0.75	0.72	0.72	
1862.5	0.054	0.051	0.105	-38.3	-27.6	0.047		0.99				
1872.5									0.93	0.82	0.82	
1877.5	0.008	0.044		0.052	-21.5	-27.4	0.038	0.01	0.21	0.92	0.91	1.17
1882.5									0.25	0.98	0.98	
1892.5	0.052	0.082	0.064	0.199	-36.0	-29.3	0.072	0.09	0.21	1.2	1.11	1.48
1902.5	0.017	0.061		0.078	-35.2	-22.5	0.054	0.03	0.13	0.94	0.91	1.12
1912.5	0.002	0.025		0.027	-33.6	-24.8	0.022	0	0.58			
1927.5	0.028	0.068	0.080	0.176	-34.8	-25.8	0.059	0.05	0.10	1.02	0.97	1.18
1932.5	0.170	0.083		0.253	-32.6	-31.7	0.072	0.3	0.98	0.77	0.47	1.82
1942.5	0.047	0.055		0.102	1.6	-22.8	0.048	0.08	0.15	0.94	0.86	1.14
1952.5	0.004	0.064	0.063	0.130	-29.9	-27.9	0.055	0.01	0.27	0.96	0.95	1.29
1962.5									0.98	0.84	0.84	
1967.5	0.006	0.053		0.059	33.0	-23.2	0.046	0.01	0.15	0.87	0.86	1.07
1972.5									0.95	0.89	0.89	
1982.5									0.26	1.05	1.05	
1987.5	0.280	0.221	0.188	0.689	4.6	0.3	0.192	0.49	0.28	0.86	0.37	1.33
1992.5									1.32	1.39	1.39	

1997.5									1.07	0.93	0.93	
2002.5	0.169	0.118		0.287	27.5	15.9	0.103	0.29	0.78	1.04	0.75	1.92
2007.5									0.25	0.93	0.93	
2012.5	0.029	0.029		0.058	-11.2	-11.7	0.026	0.05	1.13	0.9	0.85	2.06
2017.5												
2022.5	0.013	0.071		0.084	0.1	-6.2	0.062	0.02	0.18	0.95	0.93	1.19
2027.5									0.79	0.98	0.98	
2032.5	0.303	0.245	0.172	0.719	28.1	20.8	0.213	0.53				
2037.5			0.034	0.034					1.12	1.08	1.08	
2042.5	0.003	0.054	0.009	0.065	-20.1	-18.2	0.047	0.01	1.07			
2047.5												
2052.5	0.028	0.067		0.096	-24.7	-18.7	0.059	0.05	1.14	0.91	0.86	2.11
2057.5												
2062.5	0.009	0.064	0.048	0.120	-24.5	-19.3	0.056	0.01	0.16	1.02	1.01	1.24
2067.5									1.13	0.95	0.95	
2077.5	0.004	0.036		0.040	-21.8	-18.4	0.031	0.01	1.04	1.12	1.11	2.19
2082.5									1.03	1.09	1.09	
2092.5									0.35	1.14	1.14	
2097.5	0.009	0.051	0.078	0.138	-30.4	-18.2	0.044	0.02	0.98	0.97	0.95	2.00
2102.5	0.007	0.041		0.048	-19.5	-20.4	0.036	0.01	1.31	0.9	0.89	2.25
2112.5		0.026	0.021	0.046		-17.6	0.023		1.10	1.01	1.01	2.13
2117.5												
2122.5	0.042	0.066		0.108	-21.5	-14.6	0.058	0.07	1.07	0.89	0.82	2.02
2132.5		0.025		0.025		-13.2	0.022		1.21	1.03	1.03	2.26
2142.5	0.293	0.169	0.253	0.715	64.4	39.0	0.147	0.51				
2147.5		0.007		0.007		-1.9	0.006		1.01	1.08	1.08	2.10
2152.5		0.016		0.016		-10.2	0.014		1.26	1.04	1.04	2.31
2162.5	0.005	0.053	0.099	0.158	-18.2	-13.2	0.046	0.01				
2167.5	0.060	0.077		0.137	0.9	-3.6	0.067	0.1	0.95	0.85	0.75	1.86
2172.5		0.029		0.029	-13.9	-10.9	0.025		1.29	0.82	0.82	2.14
2182.5									0.28	0.87	0.87	
2187.5	0.059	0.079	0.063	0.200	7.6	-5.9	0.069	0.1	0.31	0.93	0.83	1.31
2197.5		0.011	0.124	0.135		-7.0	0.009		0.17	0.78	0.78	0.96
2207.5									0.36	1.1	1.1	
2217.5	0.168	0.174		0.342	17.7	6.8	0.152	0.29	0.25	1.28	0.99	1.68
2232.5	0.044	0.077		0.121	-15.6	-10.5	0.067	0.08	0.94	1.02	0.94	2.03
2242.5									1.06	0.83	0.83	
2247.5	0.071	0.056		0.127	-10.7	-10.1	0.049	0.12	0.80	1.17	1.05	2.02
2252.5	0.060	0.070	0.080	0.211	-5.8	-7.6	0.061	0.11	0.79	0.94	0.83	1.79
2257.5	0.094	0.083		0.177	24.7	12.1	0.072	0.16	0.21	1.18	1.02	1.47
2262.5	0.016	0.038		0.053	-9.0	-8.7	0.033	0.03	1.15			
2272.5									1.16	1.16	1.16	
2277.5	0.028	0.048	0.129	0.205	7.4	-0.8	0.042	0.05	0.20	1.13	1.08	1.37
2287.5									1.09	0.94	0.94	

2297.5	0.633	0.244		0.877	8.3	3.7	0.213	1.1	1.13	1.15	0.05	2.50
2307.5									1.05	0.81	0.81	
2317.5	0.021	0.091		0.112	-9.8	-11.1	0.079	0.04	1.24			
2322.5									0.27	0.83	0.83	
2332.5	0.026	0.058	0.086	0.171	-11.1	-9.2	0.051	0.05	1.05	0.99	0.94	2.09
2342.5	0.002	0.024		0.025	-8.9	-6.2	0.021	0	0.19	1	1	1.21
2352.5	0.035	0.049	0.023	0.107	-8.7	-8.5	0.043	0.06	0.19	0.9	0.84	1.13
2362.5										1.01	1.01	
2367.5	0.017	0.028		0.045	18.4	5.3	0.025	0.03	1.25			
2382.5	0.015	0.049		0.064	-6.1	-6.2	0.043	0.03	0.20	1.15	1.12	1.39
2397.5	0.001	0.050		0.051	-2.6	-4.8	0.043	0	0.29	0.88	0.88	1.21
2402.5	0.107	0.097		0.204	27.7	16.3	0.084	0.19	0.33	1.1	0.91	1.52
2412.5	0.218	0.290	0.245	0.752	18.6	15.7	0.252	0.38	1.07	1.39	1.01	2.71
2417.5	0.003	0.037		0.041	0.4	-3.3	0.032	0.01	1.01	1	0.99	2.05
2427.5									0.29	1.07	1.07	
2437.5	0.034	0.110	0.107	0.252	24.4	16.8	0.096	0.06	0.17			
2442.5		0.021		0.021		-1.3	0.019		1.01	0.91	0.91	1.93
2452.5		0.008	0.003	0.011		-1.7	0.007		1.14	0.87	0.87	2.01
2462.5	0.017	0.045		0.062	3.2	-1.7	0.039	0.03	1.05	0.86	0.83	1.95
2472.5		0.034		0.034		-5.7	0.029		0.29	0.99	0.99	1.31
2482.5	0.021	0.115	0.037	0.173	27.9	12.6	0.100	0.04	0.17	1.21	1.17	1.48
2492.5	0.016	0.022		0.038	12.4	1.3	0.019	0.03	0.75	0.97	0.94	1.74
2502.5		0.010		0.010		3.1	0.009		0.17	1.14	1.14	1.32
2512.5	0.013	0.047		0.060	8.7	2.9	0.041	0.02	1.04	0.85	0.83	1.94
2522.5		0.019	0.026	0.045	9.6	1.5	0.017		1.09			
2527.5	0.044	0.115		0.159	24.0	11.3	0.100	0.08	1.04	0.94	0.86	2.08
2532.5	0.016	0.047		0.062	6.6	-1.8	0.041	0.03	1.19	0.82	0.79	2.05
2542.5	0.426	0.184		0.610	31.9	22.4	0.160	0.74	0.89	1.43	0.69	2.48
2552.5	0.008	0.004	0.002	0.014		4.4	0.003	0.01	1.00	1.07	1.06	2.07
2562.5		0.145		0.145		0.2	0.127		0.16	1.14	1.14	1.43
2572.5	0.020	0.041		0.061	10.9	2.7	0.036	0.04	1.15	0.99	0.95	2.17
2577.5		0.093	0.002	0.094		-1.5	0.081		0.20	1.16	1.16	1.45
2592.5		0.154		0.154		1.4	0.134		1.13	0.99	0.99	2.25
2597.5					8.1	1.8			1.10	1.01	1.01	
2602.5	0.018	0.045		0.064	16.4	5.6	0.040	0.03	1.04	0.98	0.95	2.06
2612.5		0.140		0.140		2.0	0.122		0.19	1.28	1.28	1.59
2617.5	0.014	0.027		0.042	-1.2	7.6	0.024	0.02	1.07	1.01	0.99	2.11
2622.5	0.016	0.017	0.038	0.071	-0.5	3.5	0.015	0.03	1.00			
2632.5	0.142	0.131		0.273	19.1	5.5	0.114	0.25	1.10	1.02	0.77	2.24
2637.5	0.033	0.083		0.116	44.3	23.8	0.072	0.06	0.15	1.16	1.1	1.38
2647.5			0.003	0.003						1.06	1.06	
2652.5		0.005	0.002	0.006		3.9	0.004		1.22			
2657.5	0.115	0.095		0.210	34.6	13.9	0.082	0.2	0.24	1.32	1.12	1.64
2677.5	0.003	0.055		0.058	14.2	7.0	0.048	0.01	1.08	1.11	1.1	2.24

2687.5									1.12	1.07	1.07	
2697.5					17.8	6.7			1.11	1.11		
2702.5									0.96	0.85	0.85	
2707.5												
2712.5									0.29	1.07	1.07	
2717.5	0.053	0.100	0.010	0.163	48.7	19.3	0.087	0.09	1.04	1.2	1.11	2.32
2732.5		0.008		0.008			0.007		0.26	1.04	1.04	1.30
2747.5	0.004	0.004	0.002	0.010	20.7	10.5	0.003	0.01	1.10	0.95	0.94	2.05
2762.5	0.008	0.065		0.073	31.1	11.8	0.057	0.01	0.86	0.81	0.8	1.73
2772.5		0.037		0.037	24.0	7.5	0.032		0.17	1.17	1.17	1.37
2782.5	0.004	0.007	0.019	0.030	25.4	14.6	0.006	0.01	0.18	1.09	1.08	1.27
2792.5	0.007	0.057		0.064	20.5	5.5	0.049	0.01	1.00	1	0.99	2.05
2802.5	0.006	0.031	0.003	0.040	26.8	11.8	0.027	0.01	0.33	0.97	0.96	1.33
2812.5									1.14			
2822.5	0.006	0.011	0.007	0.024	31.2	5.3	0.009	0.01	1.02	1.17	1.16	2.20
2837.5	0.030	0.056		0.086	45.5	22.9	0.049	0.05	0.17	1.06	1.01	1.27
2847.5									0.28	0.87	0.87	
2852.5	0.028	0.046	0.101	0.175	23.8	6.8	0.040	0.05	0.90	0.73	0.68	1.67
2862.5		0.027		0.027	26.0	13.0	0.024		0.96	1.04	1.04	2.02
2872.5	0.006	0.025	0.006	0.038	30.1	8.6	0.022	0.01	0.96	1.17	1.16	2.15
2882.5		0.007		0.007		11.2	0.006		1.21	1.12	1.12	2.33
2892.5		0.006		0.006	14.0	8.5	0.005		1.15	0.91	0.91	2.06
2907.5	0.022	0.089	0.020	0.132	59.2	39.4	0.078	0.04	0.83	1.05	1.01	1.96
2912.5						16.4			0.20	1.22	1.22	
2922.5		0.036		0.036	31.9	22.2	0.031		1.15	0.95	0.95	2.13
2932.5		0.005		0.005		23.8	0.005		0.93	1.06	1.06	2.00
2942.5		0.009	0.001	0.010		11.4	0.008		1.25	1.07	1.07	2.32
2952.5		0.004		0.004		15.8	0.003		0.27	1.04	1.04	1.32
2962.5		0.020		0.020		22.8	0.018		0.17	1	1	1.19
2972.5		0.029	0.003	0.032	11.5	6.5	0.025		0.24	0.9	0.9	1.16
2982.5	0.012	0.006		0.018	19.4	13.5	0.005	0.02	0.25	0.94	0.92	1.20
2992.5									0.32	1.05	1.05	
2997.5		0.027	0.012	0.039		17.0	0.023		0.76	0.71	0.71	1.50